photonics

MDPI

Review

Robust Synthesis of Higher-Order Polarization States Through Partial-Coherence Engineering

Yue Sun [1,†], Yin Zhang [1,†], Xudong Yan [1,†], Zhongyi Hu [1], Jiahui Shen [1], Fei Wang [1], Yangjian Cai [2] and Yahong Chen [1,*]

[1] School of Physical Science and Technology, Soochow University, Suzhou 215006, China
[2] Shandong Provincial Key Laboratory of Light Field Manipulation Physics and Applications, School of Physics and Optoelectronics, Shandong Normal University, Jinan 250358, China
* Correspondence: yahongchen@suda.edu.cn
† These authors contributed equally to this work.

Abstract

Higher-order polarization states, arising from the nonseparable coupling between the spatial and polarization degrees of freedom, have important applications in structured-light science. However, when directly carried by fully coherent beams, their spatial polarization distributions are readily distorted by atmospheric turbulence, obstructions, and other propagation disturbances. This review discusses partial-coherence engineering as an alternative strategy for robust polarization-state synthesis. In this approach, a prescribed higher-order polarization state is encoded into the two-point coherence structure of a partially coherent vector source and subsequently reconstructed through propagation. We review the description of higher-order Poincaré-sphere states, their behavior in atmospheric turbulence, and the theoretical foundations of vectorial spatial coherence engineering. We then explain how coherence-to-polarization conversion enables the target state to emerge in the far field, a focal plane, or a prescribed propagation plane and compare representative experimental implementations. Finally, we assess current limitations and outline future directions and potential applications of robust higher-order polarization states. Overall, partial coherence emerges as an active degree of freedom for the robust synthesis and transmission of spatially structured polarization.

Keywords: optical coherence; polarization of light; vector beams; spatial coherence engineering; atmospheric turbulence; structured light

1. Introduction

Polarization is a fundamental property of light that describes the temporal trajectory of the electric-field vector at a given point in space [1–4]. In a conventional scalar beam, the polarization state is spatially uniform and can be separated from the scalar field amplitude. By contrast, an optical vector beam exhibits a spatially varying polarization state arising from a nonseparable coupling between its spatial and polarization degrees of freedom [5,6]. This coupling produces rich polarization textures, singularities, and spin–orbit structures that have stimulated extensive research in structured light [7–13]. Vector beams display distinctive propagation, focusing, and light–matter-interaction properties and have enabled applications in high-dimensional optical communication, polarization-sensitive imaging and sensing, optical trapping and manipulation, laser processing, and classical analogues of quantum information protocols [14].

Received: 16 September 2026
Revised: 8 October 2026
Accepted: 9 October 2026
Published: 13 October 2026

Copyright: © 2026 by the authors. Licensee MDPI, Basel, Switzerland. This article is an open access article distributed under the terms and conditions of the Creative Commons Attribution (CC BY) license.

A particularly important class of vector beams is formed by higher-order Poincaré-sphere states [15], in which two orthogonally polarized spatial modes, commonly Laguerre–Gaussian modes carrying different orbital angular momenta, are coherently superposed. The higher-order Poincaré sphere provides a unified geometrical description of scalar vortex modes, cylindrical vector beams, and their intermediate elliptically polarized states. In addition to their spatially resolved polarization distributions, these beams possess a global spatial–polarization nonseparability that can be quantified using optical concurrence [16–20]. The combination of structured polarization, orbital angular momentum, and modal nonseparability makes higher-order polarization states attractive for mode-division multiplexing, precision metrology, channel characterization, and the classical implementation of quantum-inspired protocols [21–29].

Most higher-order polarization states are synthesized with highly spatially coherent laser beams [30–35], for which the desired information is carried directly by a deterministic complex field. This direct encoding also creates a vulnerability: an obstruction removes a portion of the field [36,37], while atmospheric turbulence introduces random phase modulation, beam wander, scintillation, and coupling among spatial modes [38–43]. Although an isotropic phase-only channel acts identically on the two polarization components, the components generally occupy different spatial modes and consequently evolve into different local amplitude and phase distributions. The received spatial polarization texture may therefore be severely distorted. An instantaneous realization can remain locally fully polarized, whereas averaging over time-dependent channel realizations produces apparent depolarization. At the same time, global quantities such as concurrence may remain invariant under an ideal polarization-independent unitary channel [16,20]. These observations emphasize that preservation of a global invariant, reduced scintillation, and direct recovery of the original local polarization pattern are distinct notions of robustness.

Several strategies have been developed to mitigate turbulence-induced degradation, including adaptive optics, digital wavefront correction, transmission eigenmodes, and information encoding in channel invariants [44–49]. These methods can provide substantial improvements, but they often require instantaneous channel estimation, active feedback, multiple measurements, or prior knowledge of the perturbing medium. Their performance can also deteriorate when the channel varies faster than the correction system or when finite apertures and losses render the effective transformation nonunitary. The direct reconstruction of a prescribed higher-order polarization distribution through an unknown and dynamically varying channel therefore remains challenging.

Partially coherent light offers a complementary route. A partially coherent beam can be represented as an incoherent superposition of multiple coherent or random modes [50–53]. If many statistically independent source realizations are integrated while the turbulent channel remains approximately frozen, their incoherent averaging suppresses intensity fluctuations and beam wander within each channel realization [54–56]. Merely reducing the coherence of a conventional vector beam, however, does not guarantee preservation of its polarization structure. Different incoherent vector modes may acquire different polarization distributions during propagation, so their superposition can generate a strong unpolarized background and reduce the local degree of polarization [57–60]. The target polarization information may then be retained only weakly in the fully polarized constituent and become difficult to detect.

Spatial coherence engineering addresses this challenge by treating the two-point coherence matrix as an active carrier of structured information [61–63]. Instead of being directly imposed on the deterministic field, a prescribed higher-order polarization state is encoded into the correlation functions of a partially coherent vector source [64–69]. Subsequent propagation converts these engineered two-point correlations into a one-point polarization

matrix, allowing the target state to emerge with high polarization purity in a designated observation plane. When the source coherence area is sufficiently small, the reconstruction is governed predominantly by the encoded statistical correlations and can therefore remain stable against substantial amplitude obstructions and random phase perturbations.

Previous reviews have separately addressed vector beams and structured light [7–9,14], structured-light propagation through atmospheric turbulence [42,43], and partially coherent beams and spatial-coherence engineering [56,61–63]. However, the use of engineered two-point coherence structures for the robust synthesis of higher-order polarization states has not been reviewed systematically. The present review bridges these topics by providing a unified account of the encoding, propagation-mediated reconstruction, and robustness of such states.

In this review, we examine the physical principles, propagation mechanisms, and experimental development of robust higher-order polarization-state synthesis through partial-coherence engineering. We first introduce higher-order polarization states and clarify the distinct effects of atmospheric turbulence on their local polarization textures, ensemble-averaged properties, Stokes fluctuations, and global spatial–polarization nonseparability. We then discuss the realizability and representation of electromagnetic cross-spectral density matrices, explain the propagation-mediated conversion from coherence to polarization, and compare the principal experimental strategies for engineering partially coherent vector sources. Finally, we evaluate the scope and limitations of the reported robustness, outline future directions, and discuss the potential applications in optical communication, sensing, imaging, and manipulation.

2. Higher-Order Polarization States

A deterministic polarization state at a given spatial point can be described by a normalized Jones vector of the general form

$$\hat{\mathbf{e}} = a_1\hat{\mathbf{e}}_1 + a_2\hat{\mathbf{e}}_2, \tag{1}$$

where a_1 and a_2 are complex coefficients satisfying $|a_1|^2 + |a_2|^2 = 1$, and $\hat{\mathbf{e}}_1$ and $\hat{\mathbf{e}}_2$ are two orthogonal unit polarization vectors. Apart from a physically irrelevant global phase, any pure polarization state can be represented by a point on the Poincaré sphere, as illustrated in Figure 1a. Antipodal points on the sphere correspond to mutually orthogonal polarization states.

For a scalar optical beam, the polarization state is uniform across the transverse plane. Its electric field (spatial part) can therefore be written in the separable form

$$\mathbf{E}(\mathbf{r}) = u(\mathbf{r})\hat{\mathbf{e}}, \tag{2}$$

where $\mathbf{r} = (x, y)$ is the transverse position vector, $u(\mathbf{r})$ is a scalar complex amplitude, and $\hat{\mathbf{e}}$ is independent of position. For a vector beam, by contrast, the polarization state varies across the transverse plane. The field can, in general, be expressed as [20]

$$\mathbf{E}(\mathbf{r}) = u_1(\mathbf{r})\hat{\mathbf{e}}_1 + u_2(\mathbf{r})\hat{\mathbf{e}}_2. \tag{3}$$

When $u_1(\mathbf{r})$ and $u_2(\mathbf{r})$ cannot be written as the same scalar spatial function multiplied by two constant coefficients, the spatial and polarization degrees of freedom are nonseparable. Equation (3) then has the same mathematical structure as an entangled state in a bipartite quantum system. Vector beams possessing this form of nonseparability are therefore often referred to as classically entangled beams [70]. They have attracted considerable interest in

optical communication, precision metrology, quantum-process enhancement with classical light, and classical analogues of quantum-information protocols.

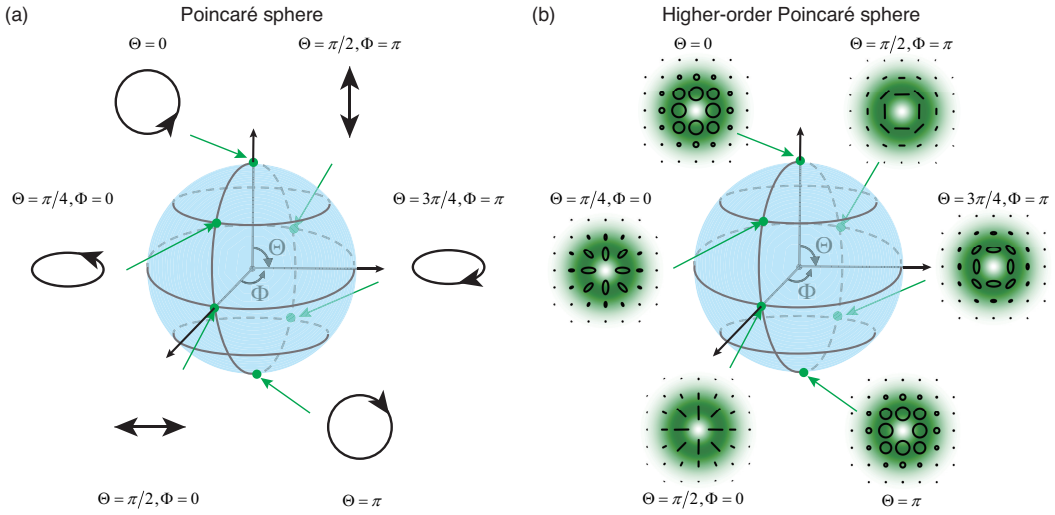


Figure 1. Geometrical representations of conventional and higher-order polarization states. (**a**) Conventional Poincaré sphere, on which each point represents a spatially uniform pure polarization state determined by the polar and azimuthal angles Θ and Φ, respectively. Antipodal points correspond to mutually orthogonal polarization states. (**b**) Higher-order Poincaré sphere for $l_1 = -l_2 = 1$ and $p_1 = p_2 = 0$. The north and south poles represent orthogonally polarized scalar Laguerre–Gaussian modes carrying opposite orbital angular momenta, whereas all other points represent their nonseparable superpositions. States on the equator are maximally nonseparable vector beams, including the radial and azimuthal polarization states at $(\Theta, \Phi) = (\pi/2, 0)$ and $(\pi/2, \pi)$, respectively, while intermediate latitudes correspond to partially nonseparable vector states with $C = \sin\Theta$. The green distributions indicate the beam intensity, and the black curves and line segments show the local polarization ellipses.

The degree of nonseparability between the spatial and polarization degrees of freedom can be quantified by the concurrence. This quantity was originally introduced by Wootters in quantum information theory as a measure of entanglement for two-qubit systems [71,72]. Owing to the mathematical analogy between a bipartite quantum state and the nonseparable spatial–polarization structure of a vector beam, McLaren, Konrad, and Forbes subsequently adapted concurrence to classical vector optical fields [73]. In this classical context, concurrence quantifies the vectorness, or equivalently the degree of nonseparability, of the beam rather than genuine quantum entanglement [74]. For the field in Equation (3), the optical concurrence is defined as [20]

$$C = \frac{2\sqrt{(u_1, u_1)(u_2, u_2) - |(u_1, u_2)|^2}}{(u_1, u_1) + (u_2, u_2)}, \tag{4}$$

where $(u_i, u_j) = \int u_i^*(\mathbf{r}) u_j(\mathbf{r})\, \mathrm{d}^2\mathbf{r}$ denotes the spatial inner product. The concurrence satisfies $0 \leq C \leq 1$. A value of $C = 0$ corresponds to a separable scalar beam, whereas $C = 1$ represents a maximally nonseparable vector beam.

A particularly important family of vector beams consists of those carrying higher-order Poincaré-sphere (HOPS) polarization states [33]. A general HOPS state can be written as

$$\mathbf{E}(\mathbf{r}) = \cos\left(\frac{\Theta}{2}\right) \exp\left(-\mathrm{i}\frac{\Phi}{2}\right) \mathrm{LG}_{p_1,l_1}(\mathbf{r})\hat{\mathbf{e}}_1 + \sin\left(\frac{\Theta}{2}\right) \exp\left(\mathrm{i}\frac{\Phi}{2}\right) \mathrm{LG}_{p_2,l_2}(\mathbf{r})\hat{\mathbf{e}}_2, \tag{5}$$

where $\mathrm{LG}_{p,l}(\mathbf{r})$ denotes a (power-normalized) Laguerre–Gaussian mode with radial index p and azimuthal index l. The azimuthal index determines the orbital angular momentum

carried by the mode, with each photon possessing an orbital angular momentum of $l\hbar$ [75]. The parameters $\Theta \in [0, \pi]$ and $\Phi \in [0, 2\pi)$ determine, respectively, the relative amplitudes and phase of the two constituent modes.

The state in Equation (5) can be represented by a point on a higher-order Poincaré sphere, as shown in Figure 1b, where Θ and Φ are the polar and azimuthal angles. The north and south poles correspond to the basis states $\mathrm{LG}_{p_1,l_1}\hat{\mathbf{e}}_1$ and $\mathrm{LG}_{p_2,l_2}\hat{\mathbf{e}}_2$, respectively, while all other points represent their coherent superpositions. In the conventional construction, the two poles are typically associated with right- and left-circularly polarized modes carrying opposite orbital angular momenta.

If the two Laguerre–Gaussian modes are individually normalized and spatially orthogonal, namely, $\int \mathrm{LG}^*_{p_1,l_1}(\mathbf{r})\mathrm{LG}_{p_2,l_2}(\mathbf{r})\,\mathrm{d}^2\mathbf{r} = 0$, the concurrence of the HOPS state reduces to

$$C = \sin\Theta. \tag{6}$$

Consequently, states on the equator of the higher-order Poincaré sphere, for which $\Theta = \pi/2$, are maximally nonseparable vector states with $C = 1$. The two poles, corresponding to $\Theta = 0$ and $\Theta = \pi$, are separable scalar states with $C = 0$. Intermediate points obey $0 < C < 1$.

3. Higher-Order Polarization States in Atmospheric Turbulence

Atmospheric turbulence produces random fluctuations in the refractive index of air and consequently perturbs the amplitude, phase, and spatial structure of a propagating optical beam. Under the paraxial approximation, a monochromatic vector field propagating through atmospheric turbulence obeys the stochastic parabolic wave equation [76]

$$2\mathrm{i}k\frac{\partial \mathbf{E}(\mathbf{r},z,t)}{\partial z} + \nabla_\perp^2\,\mathbf{E}(\mathbf{r},z,t) + 2k^2\delta n(\mathbf{r},z,t)\mathbf{E}(\mathbf{r},z,t) = 0, \tag{7}$$

where $k = 2\pi/\lambda$ is the wavenumber, λ is the wavelength, z is the propagation distance, $\nabla_\perp^2 = \partial_x^2 + \partial_y^2$ is the transverse Laplacian, and $\delta n(\mathbf{r}, z, t)$ is the fluctuating part of the refractive index. The time dependence of δn describes the dynamical evolution of the turbulent atmosphere.

For an isotropic and nonbirefringent atmosphere, turbulence does not act directly on the polarization basis. Substitution of Equation (3) into Equation (7) shows that the two scalar spatial amplitudes obey the same stochastic propagation equation,

$$2\mathrm{i}k\frac{\partial u_j(\mathbf{r},z,t)}{\partial z} + \nabla_\perp^2 u_j(\mathbf{r},z,t) + 2k^2\delta n(\mathbf{r},z,t)u_j(\mathbf{r},z,t) = 0, \qquad j \in \{1,2\}. \tag{8}$$

Although the same turbulent operator acts on both components, their initial spatial modes are generally different. The two components therefore evolve into different spatial distributions, causing their local amplitude ratio and relative phase to vary during propagation. Because the local polarization state is determined by these two quantities, such turbulence-induced variations ultimately distort the spatial polarization distribution of the vector beam.

For the qth realization of turbulence, let $\mathcal{T}_q$ denote the corresponding propagation operator. Without repeating the incident field already defined in Equation (3), the field in the receiver plane can be written as

$$\mathbf{E}_{q,\mathrm{out}}(\mathbf{r}) = v_{1,q}(\mathbf{r})\hat{\mathbf{e}}_1 + v_{2,q}(\mathbf{r})\hat{\mathbf{e}}_2, \tag{9}$$

where

$$v_{j,q}(\mathbf{r}) = \mathcal{T}_q\big[u_j(\mathbf{r})\big], \qquad j \in \{1,2\}. \tag{10}$$

Representative instantaneous polarization distributions in the receiver plane are shown in Figure 2a,b for two turbulence strengths quantified by the Rytov variance σ_R^2. Conventionally, $\sigma_R^2 < 1$ corresponds to the weak-fluctuation regime, whereas $\sigma_R^2 \gtrsim 1$ indicates moderate-to-strong turbulence [76]. Turbulence produces random phase distortions, beam wander, and intensity scintillation. The characteristic intensity and polarization texture of the incident higher-order polarization state is therefore distorted, and the distortion generally becomes more severe as the turbulence strength increases.

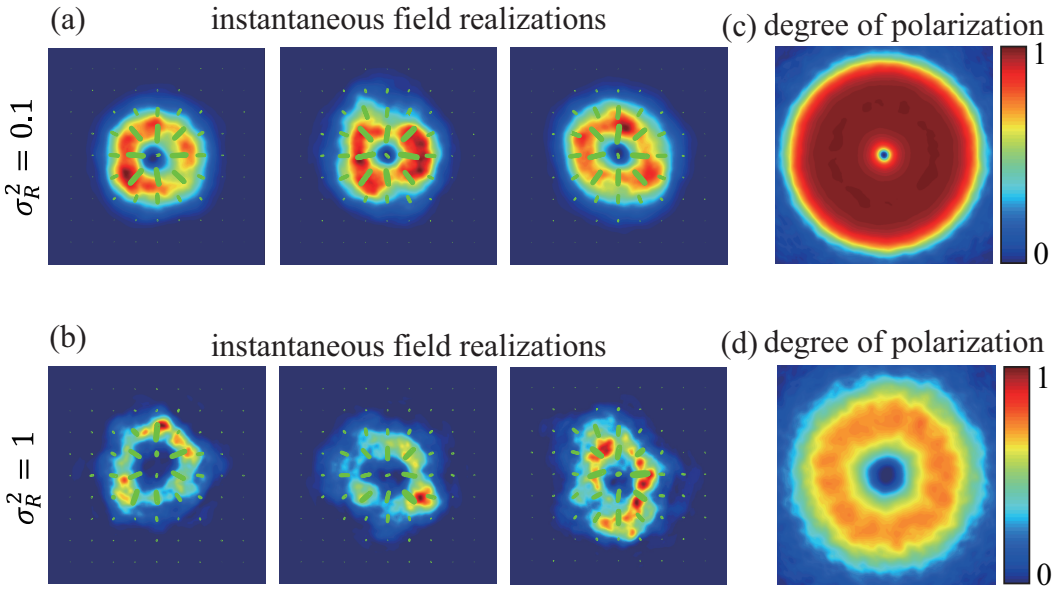


Figure 2. Effects of atmospheric turbulence on a radially polarized beam in the receiver plane. (**a**,**b**) Representative instantaneous intensity and polarization distributions for Rytov variances $\sigma_R^2 = 0.1$ and $\sigma_R^2 = 1$, respectively. The overlaid polarization ellipses indicate that each instantaneous realization remains locally fully polarized, although its intensity and spatial polarization texture become increasingly distorted as the turbulence strength increases. (**c**,**d**) Corresponding spatial distributions of the degree of polarization calculated from the ensemble-averaged polarization matrix. Stronger turbulence produces more pronounced statistical depolarization and a greater reduction in the local degree of polarization.

For each fixed realization of an isotropic phase-only turbulent channel, the field in Equation (9) remains a deterministic Jones field and is therefore locally fully polarized wherever its intensity is nonzero. Apparent depolarization arises when the detector performs a temporal or ensemble average over multiple time-dependent turbulence realizations. The polarization matrix of the ensemble-averaged field is defined as [50]

$$\mathbf{\Phi}(\mathbf{r}) = \left\langle \mathbf{E}_{q,\mathrm{out}}^{*}(\mathbf{r}) \mathbf{E}_{q,\mathrm{out}}^{\mathrm{T}}(\mathbf{r}) \right\rangle_q, \tag{11}$$

where $\langle \cdot \rangle_q$ denotes an ensemble average over turbulence realizations. The corresponding local degree of polarization is [50]

$$P(\mathbf{r}) = \left[1 - \frac{4 \det \mathbf{\Phi}(\mathbf{r})}{\mathrm{tr}^2 \mathbf{\Phi}(\mathbf{r})} \right]^{1/2} = \frac{\sqrt{\langle S_1(\mathbf{r}) \rangle_q^2 + \langle S_2(\mathbf{r}) \rangle_q^2 + \langle S_3(\mathbf{r}) \rangle_q^2}}{\langle S_0(\mathbf{r}) \rangle_q}, \tag{12}$$

where det and tr denote the determinant and trace of a matrix, respectively. The quantities $S_0(\mathbf{r})$, $S_1(\mathbf{r})$, $S_2(\mathbf{r})$, and $S_3(\mathbf{r})$ are the four local Stokes parameters associated with an individual field realization. Here, S_0 represents the total intensity, whereas S_1, S_2, and S_3 characterize the local polarization states.

As illustrated in Figure 2c,d, the degree of polarization of the ensemble-averaged beam decreases as the turbulence becomes stronger. This reduction occurs because different realizations produce different local polarization ellipses, which partially cancel the degree of polarization upon averaging.

In addition to modifying the ensemble-averaged polarization structure, atmospheric turbulence induces random fluctuations in all four Stokes parameters. For the qth turbulence realization, the fluctuation in the jth Stokes parameter with respect to its ensemble average is defined as [77]

$$\Delta S_{j,q}(\mathbf{r}) = S_{j,q}(\mathbf{r}) - \langle S_{j,q}(\mathbf{r}) \rangle_q, \qquad j \in \{0,1,2,3\}. \tag{13}$$

The corresponding local Stokes scintillation index is

$$\sigma_j^2(\mathbf{r}) = \frac{\langle [\Delta S_{j,q}(\mathbf{r})]^2 \rangle_q}{\langle S_{j,q}(\mathbf{r}) \rangle_q^2}. \tag{14}$$

Here, σ_0^2 is the conventional intensity scintillation index, whereas σ_1^2, σ_2^2, and σ_3^2 quantify the fluctuations in the polarization-dependent Stokes parameters.

The normalized indices in Equation (14) can become artificially large in regions where the mean Stokes parameter or the beam intensity approaches zero. To characterize the global fluctuations within the effective beam area, the overall Stokes scintillation is defined as [77]

$$\xi_j = \frac{1}{S_\Omega} \iint_\Omega \sigma_j^2(\mathbf{r})\, \mathrm{d}^2\mathbf{r}, \tag{15}$$

where Ω denotes the selected effective-intensity region and S_Ω is its area. In Ref. [77], Ω was chosen as the region in which the ensemble-averaged intensity exceeded 10% of its maximum value.

Numerical simulations of a radially polarized beam propagating through atmospheric turbulence showed that

$$\xi_0 > \xi_j, \qquad j \in \{1,2,3\}, \tag{16}$$

over a broad range of turbulence strengths, as shown in Figure 3. This result indicates that the polarization-dependent Stokes parameters are statistically more stable than the total intensity. Although all four overall Stokes scintillations increase with turbulence strength, the gap between the intensity scintillation and the polarization-dependent scintillations also widens. This behavior can be understood in terms of turbulence-induced statistical depolarization. The total intensity contains contributions from both the fully polarized and unpolarized parts of the ensemble-averaged beam, whereas the polarization-dependent Stokes parameters S_1, S_2, and S_3 are determined only by the fully polarized part. Consequently, fluctuations in both parts contribute to ξ_0, while only fluctuations in the polarized part contribute to ξ_1, ξ_2, and ξ_3.

The total-intensity scintillation of a vector beam can also be lower than that of either of its scalar constituent modes. This result is distinct from Equation (16): the former compares the intensity fluctuations of vector and scalar beams, whereas the latter compares the fluctuations of different Stokes parameters within the same vector beam. Together, these results demonstrate the intrinsic resilience of vector beams to atmospheric fluctuations. Nevertheless, reduced intensity or Stokes scintillation does not by itself guarantee the recovery of the original spatial polarization texture.

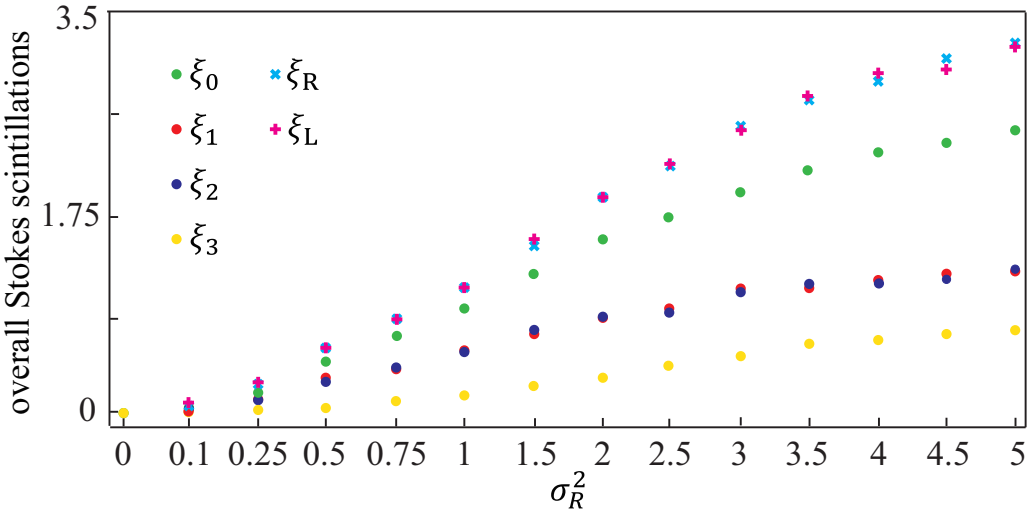


Figure 3. Overall Stokes scintillations of a radially polarized beam as functions of the Rytov variance σ_R^2. The quantities ξ_0, ξ_1, ξ_2, and ξ_3 denote the spatially averaged scintillation indices of the four Stokes parameters, whereas ξ_R and ξ_L represent the overall intensity scintillations of the constituent scalar modes $\mathrm{LG}_{0,1}(\mathbf{r})\hat{\mathbf{e}}_R$ and $\mathrm{LG}_{0,-1}(\mathbf{r})\hat{\mathbf{e}}_L$, respectively. All scintillations increase with turbulence strength, while the polarization-dependent components satisfy $\xi_1, \xi_2, \xi_3 < \xi_0$. In addition, the total-intensity scintillation of the vector beam is lower than that of either scalar constituent, demonstrating its enhanced statistical stability in atmospheric turbulence. From Ref. [77].

Atmospheric turbulence can also be described within a quantum-inspired channel framework. The vector field in Equation (3) can be represented in the product space of the spatial and polarization degrees of freedom as [16]

$$|\Psi_{\mathrm{in}}\rangle = |u_1\rangle|\hat{\mathbf{e}}_1\rangle + |u_2\rangle|\hat{\mathbf{e}}_2\rangle. \tag{17}$$

For an isotropic and polarization-independent atmosphere, turbulence acts on the spatial modes without directly modifying the polarization basis and can therefore be regarded as a one-sided channel [16]:

$$\begin{aligned} |\Psi_{q,\mathrm{out}}\rangle &= \left(\mathcal{T}_q \otimes \mathbb{I}_{\mathrm{pol}}\right)|\Psi_{\mathrm{in}}\rangle \\ &= |v_{1,q}\rangle|\hat{\mathbf{e}}_1\rangle + |v_{2,q}\rangle|\hat{\mathbf{e}}_2\rangle, \end{aligned} \tag{18}$$

where $|v_{j,q}\rangle = \mathcal{T}_q|u_j\rangle$ and $\mathcal{T}_q$ is the spatial propagation operator associated with the qth turbulence realization. When expressed in the original Laguerre–Gaussian basis, each turbulence-distorted spatial mode is generally a random superposition of modes with different radial and azimuthal indices:

$$v_{j,q}(\mathbf{r}) = \sum_{p,l} t_{pl,j}^{(q)} \mathrm{LG}_{p,l}(\mathbf{r}), \tag{19}$$

where $t_{pl,j}^{(q)} = \left(\mathrm{LG}_{p,l}, \mathcal{T}_q u_j\right)$ is the corresponding modal coupling coefficient, and the spatial inner product has been defined previously. This turbulence-induced modal coupling explains why the received intensity and polarization textures can differ substantially from those of the incident beam.

For ideal phase-only propagation with complete collection of the output field, $\mathcal{T}_q$ is unitary and satisfies

$$\mathcal{T}_q^{\dagger}\mathcal{T}_q = \mathbb{I}. \tag{20}$$

The inner products between the two spatial components are consequently preserved:

$$\begin{aligned}(v_{i,q}, v_{j,q}) &= \left(\mathcal{T}_q u_i, \mathcal{T}_q u_j\right) \\ &= \left(u_i, \mathcal{T}_q^{\dagger}\mathcal{T}_q u_j\right) \\ &= (u_i, u_j).\end{aligned} \tag{21}$$

Because all the inner products entering the concurrence in Equation (4) remain unchanged, it follows that

$$C_{q,\mathrm{out}} = C_{\mathrm{in}}. \tag{22}$$

For a HOPS state, the invariant concurrence is given by Equation (6). Thus, the global spatial–polarization nonseparability remains unchanged for each realization of a unitary one-sided channel, even though the intensity, phase, and spatially resolved polarization texture may be severely distorted.

This invariance has well-defined boundaries. It applies realization by realization to an ideal, polarization-independent unitary channel. Finite transmitter and receiver apertures, polarization-dependent loss, birefringence, multiple scattering, and genuine depolarization can make the effective channel nonunitary or cause it to act on both the spatial and polarization degrees of freedom. Moreover, an incoherent ensemble average over different unitary turbulence realizations produces a mixed field that is not described directly by the pure-state invariance proof. Preservation of the concurrence should therefore not be interpreted as preservation of the original intensity or spatial polarization distribution.

The preceding results reveal several distinct forms of robustness. First, a vector beam may exhibit lower intensity scintillation than its constituent scalar modes. Second, its polarization-dependent Stokes parameters may fluctuate less strongly than its total intensity. Third, its concurrence may remain invariant under a unitary one-sided channel. Although these properties demonstrate the intrinsic resilience of vector beams, none guarantee direct recovery of the original spatially resolved higher-order polarization state in a fixed receiver plane. Intensity and Stokes scintillations quantify statistical fluctuations and depend on the source statistics, turbulence strength, and detector averaging time, whereas concurrence is a global quantity that remains invariant only for an ideal polarization-independent unitary channel with complete field collection. Recovery of the spatially resolved polarization distribution is a stronger criterion, requiring the local polarization state in the receiver plane to reproduce the prescribed target pattern.

Transmission-eigenmode approaches can restore or protect selected field structures, but they generally require knowledge of the instantaneous channel as well as sufficiently rapid channel estimation and correction [48,78]. This limitation motivates partial-coherence engineering. Rather than relying solely on a global invariant or adapting the incident field to each turbulence realization, partial-coherence engineering encodes the target higher-order polarization state into the two-point coherence structure of a random vector source. The encoded state is subsequently released and reconstructed through propagation and statistical averaging. As discussed in the following sections, this strategy offers a route to the direct recovery of prescribed higher-order polarization textures without explicitly inverting every instantaneous realization of the turbulent channel.

4. Spatial Coherence Engineering

Higher-order polarization states have conventionally been generated using laser beams with a high degree of spatial coherence. In such fully coherent beams, the target polarization distribution is directly carried by a deterministic optical field and can therefore be severely distorted by perturbations encountered during propagation, including atmospheric tur-

bulence. By contrast, partially coherent beams with a sufficiently low spatial coherence generally exhibit enhanced robustness against turbulence-induced intensity scintillation, beam wander, and beam spreading [54–56,79,80]. This robustness can be understood from the coherent-mode representation, according to which a partially coherent beam is an incoherent superposition of multiple spatial modes. If the characteristic time of the source fluctuations, the detector integration time, and the atmospheric coherence time satisfy

$$t_{\mathrm{s}} \ll t_{\mathrm{d}} \ll t_{\mathrm{turb}}, \tag{23}$$

the detector averages over many statistically independent source realizations while the turbulent channel remains approximately frozen. This statistical averaging suppresses the channel-induced fluctuations within each fixed turbulence realization, producing a more stable received intensity distribution than that of a fully coherent beam.

A straightforward approach to combining structured polarization with partial coherence is to reduce the spatial coherence of an existing vector beam, for example, by constructing an electromagnetic Gaussian Schell-model beam [57,81]. In such beams, however, the mutually incoherent vector modes generally evolve into different spatial and polarization distributions during propagation. Their incoherent superposition can therefore reduce the local degree of polarization. Consequently, even when the fully polarized part approximately preserves the desired higher-order polarization texture, it may be embedded in a strong unpolarized background, resulting in a reduced polarization contrast and signal-to-noise ratio. The objective considered in this review is more demanding: to generate a received beam that exhibits both a high degree of polarization and a stable higher-order polarization distribution within each approximately frozen realization of the turbulent channel.

A promising strategy for achieving this objective is spatial coherence engineering of partially coherent vector light. Spatial coherence engineering refers to the deliberate modulation of the two-point spatial correlations of a random optical source to obtain desired propagation, focusing, beam-shaping, or light–matter-interaction properties [63]. Its mathematical foundation can be traced to the work of Gori and Santarsiero on the construction of genuine spatial correlation functions [82,83] and its subsequent extension to electromagnetic cross-spectral density matrices [84]. Since then, spatial coherence has developed from a passive statistical property into an actively controllable degree of freedom for structured-light synthesis [62].

For a statistically stationary, quasi-monochromatic vector beam, the second-order spatial coherence and polarization properties are characterized by the 2×2 cross-spectral density matrix [85]

$$\mathbf{W}(\mathbf{r}_1, \mathbf{r}_2) = \left\langle \mathbf{E}^*(\mathbf{r}_1)\mathbf{E}^{\mathrm{T}}(\mathbf{r}_2) \right\rangle, \tag{24}$$

whose elements are

$$W_{\alpha\beta}(\mathbf{r}_1, \mathbf{r}_2) = \left\langle E_\alpha^*(\mathbf{r}_1)E_\beta(\mathbf{r}_2) \right\rangle, \qquad \alpha, \beta \in \{x, y\}. \tag{25}$$

Here, the angle brackets denote an ensemble average over the random field realizations. At equal spatial points, $\mathbf{W}(\mathbf{r}, \mathbf{r})$ reduces to the polarization matrix $\mathbf{\Phi}(\mathbf{r})$ introduced in the preceding section.

A physically realizable cross-spectral density matrix must satisfy the Hermiticity condition [50]

$$\mathbf{W}(\mathbf{r}_1, \mathbf{r}_2) = \mathbf{W}^\dagger(\mathbf{r}_2, \mathbf{r}_1) \tag{26}$$

and the nonnegative-definiteness condition

$$\sum_{\alpha,\beta\in\{x,y\}} \iint f_\alpha^*(\mathbf{r}_1) W_{\alpha\beta}(\mathbf{r}_1,\mathbf{r}_2) f_\beta(\mathbf{r}_2)\, \mathrm{d}^2\mathbf{r}_1\, \mathrm{d}^2\mathbf{r}_2 \geq 0 \tag{27}$$

for every square-integrable vector test function $\mathbf{f}(\mathbf{r}) = [f_x(\mathbf{r}), f_y(\mathbf{r})]^{\mathrm{T}}$. This condition ensures that the energy predicted for any linear projection of the random field is nonnegative.

A broad class of physically realizable cross-spectral density matrices can be constructed using the integral representation [66]

$$W_{\alpha\beta}(\mathbf{r}_1,\mathbf{r}_2) = \int p_{\alpha\beta}(\mathbf{v}) H_\alpha^*(\mathbf{r}_1,\mathbf{v}) H_\beta(\mathbf{r}_2,\mathbf{v})\, \mathrm{d}^2\mathbf{v}, \tag{28}$$

where $\mathbf{v}$ is an auxiliary two-dimensional position or spatial-frequency variable, $H_x(\mathbf{r},\mathbf{v})$ and $H_y(\mathbf{r},\mathbf{v})$ are arbitrary well-behaved kernel functions, and $p_{\alpha\beta}(\mathbf{v})$ are the elements of a Hermitian weighting matrix

$$\mathbf{p}(\mathbf{v}) = \begin{bmatrix} p_{xx}(\mathbf{v}) & p_{xy}(\mathbf{v}) \\ p_{yx}(\mathbf{v}) & p_{yy}(\mathbf{v}) \end{bmatrix}. \tag{29}$$

For every $\mathbf{v}$, the weighting matrix must be nonnegative semidefinite. For a 2×2 Hermitian matrix, this requirement is equivalent to

$$p_{xx}(\mathbf{v}) \geq 0, \qquad p_{yy}(\mathbf{v}) \geq 0, \qquad p_{yx}(\mathbf{v}) = p_{xy}^*(\mathbf{v}), \qquad p_{xx}(\mathbf{v}) p_{yy}(\mathbf{v}) - |p_{xy}(\mathbf{v})|^2 \geq 0. \tag{30}$$

The diagonal elements of $\mathbf{p}(\mathbf{v})$ are therefore real and nonnegative, whereas its off-diagonal elements may be complex. Equations (28) and (30) provide a sufficient construction that automatically guarantees the nonnegative definiteness of $\mathbf{W}(\mathbf{r}_1,\mathbf{r}_2)$.

Equation (28) shows that the spatial coherence structure can be engineered through both the weighting matrix $\mathbf{p}(\mathbf{v})$ and the kernel functions $H_x(\mathbf{r},\mathbf{v})$ and $H_y(\mathbf{r},\mathbf{v})$. A particularly important case is obtained when the two polarization components share the Fourier-type kernel

$$H_\alpha(\mathbf{r},\mathbf{v}) = T(\mathbf{r}) \exp(\mathrm{i} c_0 \mathbf{r}\cdot\mathbf{v}), \qquad \alpha \in \{x,y\}, \tag{31}$$

where $T(\mathbf{r})$ is taken to be a real amplitude function determining the source intensity profile, and c_0 is a real scaling parameter controlling the transverse coherence width. Substitution of Equation (31) into Equation (28) gives

$$W_{\alpha\beta}(\mathbf{r}_1,\mathbf{r}_2) = T^*(\mathbf{r}_1) T(\mathbf{r}_2) \int p_{\alpha\beta}(\mathbf{v}) \exp[\mathrm{i} c_0 (\mathbf{r}_2 - \mathbf{r}_1)\cdot\mathbf{v}]\, \mathrm{d}^2\mathbf{v}. \tag{32}$$

The source constructed in this form belongs to the Schell-model family because its normalized correlation coefficients depend only on the coordinate difference $\mathbf{r}_2 - \mathbf{r}_1$.

For the α and β field components, the normalized correlation coefficient is defined as

$$\mu_{\alpha\beta}(\mathbf{r}_1,\mathbf{r}_2) = \frac{W_{\alpha\beta}(\mathbf{r}_1,\mathbf{r}_2)}{\sqrt{W_{\alpha\alpha}(\mathbf{r}_1,\mathbf{r}_1) W_{\beta\beta}(\mathbf{r}_2,\mathbf{r}_2)}}. \tag{33}$$

Defining

$$K_{\alpha\beta} = \left[\int p_{\alpha\alpha}(\mathbf{v})\, \mathrm{d}^2\mathbf{v} \int p_{\beta\beta}(\mathbf{v})\, \mathrm{d}^2\mathbf{v} \right]^{1/2}, \tag{34}$$

the normalized correlation coefficient becomes

$$\mu_{\alpha\beta}(\mathbf{r}_2 - \mathbf{r}_1) = \frac{1}{K_{\alpha\beta}} \int p_{\alpha\beta}(\mathbf{v}) \exp[\mathrm{i}c_0(\mathbf{r}_2 - \mathbf{r}_1) \cdot \mathbf{v}] \, \mathrm{d}^2\mathbf{v}. \tag{35}$$

Thus,

$$\mu_{\alpha\beta}(\mathbf{r}_2 - \mathbf{r}_1) \propto \mathcal{F}\left[p_{\alpha\beta}(\mathbf{v})\right], \tag{36}$$

where $\mathcal{F}$ denotes a two-dimensional Fourier transform, with its precise scaling and sign determined by the adopted convention. The transverse coherence width is controlled jointly by c_0 and the spatial extent of $p_{\alpha\beta}(\mathbf{v})$: increasing c_0 or broadening the weighting distribution generally reduces the coherence width.

An important consequence of Equation (36) is that the spatial information contained in the weighting matrix can be transferred into the two-point coherence structure of the partially coherent source. Since $\mathbf{p}(\mathbf{v})$ obeys the same Hermiticity and nonnegative-semidefiniteness conditions as a polarization matrix, it can be chosen to reproduce the polarization matrix of a prescribed higher-order polarization state. In this case, the target one-point polarization information is no longer directly visible in the source-plane intensity or local polarization distribution; instead, it is encoded in the four two-point correlation functions $\mu_{\alpha\beta}(\mathbf{r}_1, \mathbf{r}_2)$. As shown in the following section, suitable propagation converts these engineered correlations back into a highly polarized higher-order polarization state in the designated observation plane. This coherence-to-polarization conversion constitutes the central mechanism underlying the robust synthesis of higher-order polarization states.

5. Propagation of Spatial-Coherence-Engineered Beams

The propagation of a partially coherent vector field can be described using the Green-function formulation, in which the Green tensor acts as the spatial transfer function connecting the cross-spectral density matrices in the source and observation planes [86]. Under the paraxial approximation, this formulation reduces to the extended Collins integral, which is particularly useful for describing partially coherent beams propagating through stigmatic first-order optical systems characterized by an ABCD ray-transfer matrix [87,88]. More recently, the extended Collins integral has been recast into a convolution form, initially for scalar partially coherent beams [89] and subsequently generalized to vector [66] and three-component random fields [90,91].

Let $\mathbf{r}'$ and $\mathbf{r}$ denote the transverse position vectors in the source and observation planes, respectively. For the Schell-model source introduced in the preceding section, the propagated polarization matrix can be written as

$$\Phi_{\alpha\beta}^{(z)}(\mathbf{r}) = \frac{K_{\alpha\beta}}{(\lambda B)^2} \left[\left| \widetilde{\mathcal{A}}\left(\frac{\mathbf{r}}{\lambda B}\right) \right|^2 \otimes \widetilde{\mu}_{\alpha\beta}\left(\frac{\mathbf{r}}{\lambda B}\right) \right], \qquad \alpha, \beta \in \{x, y\}, \tag{37}$$

where λ is the wavelength, A and B are elements of the ABCD matrix, the tilde denotes a two-dimensional Fourier transform, and $\otimes$ denotes convolution with respect to the spatial-frequency coordinate. The generalized source amplitude appearing in Equation (37) is

$$\mathcal{A}(\mathbf{r}') = T(\mathbf{r}') \exp\left(\frac{\mathrm{i}kA}{2B}|\mathbf{r}'|^2\right), \tag{38}$$

where $k = 2\pi/\lambda$. Equation (37) shows that the propagated intensity and polarization distributions are jointly determined by the source amplitude $T(\mathbf{r}')$ and the engineered correlation coefficients $\mu_{\alpha\beta}(\mathbf{r}_2 - \mathbf{r}_1)$.

When the spatial coherence width is sufficiently small, i.e., the spatial coherence area is much smaller than the beam area, $\widetilde{\mu}_{\alpha\beta}$ varies much more slowly than $|\widetilde{\mathcal{A}}|^2$. In this limit,

$|\widetilde{\mathcal{A}}|^2$ acts as a narrow convolution kernel and the polarization matrix is approximately proportional to the Fourier transform of the source correlation matrix:

$$\Phi_{\alpha\beta}^{(z)}(\mathbf{r}) \propto \widetilde{\mu}_{\alpha\beta}\left(\frac{\mathbf{r}}{\lambda B}\right). \tag{39}$$

This approximation implies that the polarization structure is governed predominantly by the engineered spatial correlations.

Combining Equation (39) with Equation (36) gives

$$\Phi_{\alpha\beta}^{(z)}(\mathbf{r}) \propto p_{\alpha\beta}\left(\frac{\mathbf{r}}{a_0\lambda B}\right), \tag{40}$$

up to a coordinate inversion, normalization factor, and scaling determined by the adopted Fourier-transform convention. Because the weighting matrix $\mathbf{p}(\mathbf{v})$ is chosen to reproduce the polarization matrix of the target higher-order polarization state, propagation converts the two-point coherence information into a directly observable one-point polarization distribution. The encoded polarization state is therefore progressively released from the spatial coherence structure and reconstructed in the designed observation plane.

Figure 4a,b compare the focusing behavior of a conventional partially coherent radially polarized beam with that of a spatial-coherence-engineered beam. For the conventional beam, the mutually incoherent spatial modes develop different polarization distributions during propagation, and their incoherent superposition leads to a progressive reduction in the degree of polarization [57]. For the spatial-coherence-engineered beam, by contrast, propagation converts the encoded correlations into the prescribed polarization matrix. Consequently, the degree of polarization increases as the beam approaches the focal plane, where a higher-order polarization state with high polarization purity is reconstructed [66]. In the ordinary Fourier-encoding scheme, the target state is therefore recovered in the focal plane of a lens or, equivalently, in the far field of a freely propagating beam.

The Fourier kernel in Equation (31) represents only one possible realization of spatial coherence engineering. More general kernels can be constructed using fractional Fourier transforms (FrFTs), allowing the encoded polarization state to emerge at a prescribed finite propagation distance rather than only in the focal or far-field plane [92]. In this approach, mutually uncorrelated vector modes carrying different linear phase factors are processed by an FrFT system. Immediately after the FrFT system, these modes are transversely displaced and their incoherent superposition forms a spatially partially coherent and partially polarized source. During subsequent propagation, the displaced modes gradually overlap and become synchronized, producing a deterministic higher-order polarization state in a designed plane.

For free-space propagation following an FrFT system of fractional order p_E, the distance at which the deterministic polarization state emerges is [92]

$$z_c = z_R \tan\left(\frac{\pi p_E}{2}\right), \tag{41}$$

where z_R is the Rayleigh range of the constituent modes. When a thin lens of focal length f is included immediately after the synthesized source, the corresponding distance is determined by

$$\frac{1}{z_c} = \frac{1}{f} + \frac{1}{z_R \tan(\pi p_E/2)}. \tag{42}$$

In the limiting case $p_E = 1$, the FrFT becomes an ordinary Fourier transform and $z_c \to \infty$ in free space, so that the deterministic polarization state appears only in the far field.

For $0 < p_E < 1$, however, z_c is finite and can be continuously controlled through the fractional order.

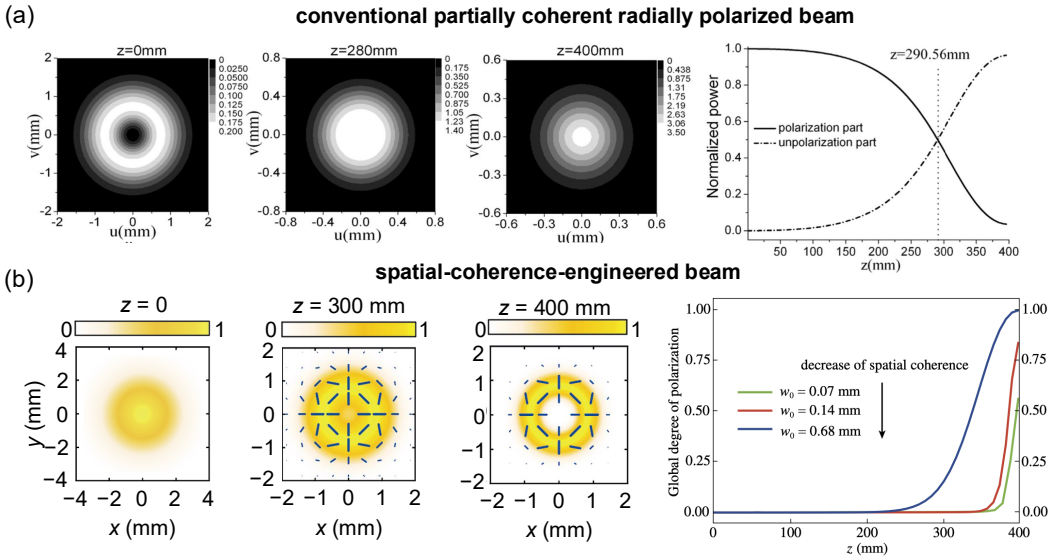


Figure 4. Contrasting polarization evolution of conventional and spatial-coherence-engineered partially coherent vector beams during focusing. (**a**) Transverse intensity distributions of a conventional Gaussian Schell-model radially polarized beam at different distances during focusing. The right panel shows the normalized powers of its polarized and unpolarized components as functions of propagation distance. The polarized contribution decreases while the unpolarized contribution increases, demonstrating propagation-induced depolarization. (**b**) Intensity and polarization distributions of a spatial-coherence-engineered beam in which a higher-order polarization state is encoded into the source coherence structure. The encoded polarization state gradually emerges during propagation and is reconstructed with high polarization purity in the focal plane at $z = 400$ mm. The right panel shows the global degree of polarization, defined as the ratio of the power carried by the fully polarized component to the total beam power, for different beam radii w_0 on the rotating ground-glass disk. Increasing w_0, corresponding to a smaller source coherence width, promotes the coherence-to-polarization conversion and enables the global degree of polarization to approach unity in the focal plane. Adapted from Refs. [57,66].

Figure 5 illustrates the evolution of the intensity, spatial polarization distribution, local degree of polarization, and overall polarization purity of such a beam. Although the source is initially partially polarized, its polarization purity increases during propagation and reaches unity at the designed plane. For the representative parameters $f = 400$ mm, $z_R \simeq 531.2$ mm, and $p_E = 0.41$, Equation (42) gives $z_c = 200$ mm, which lies before the focal plane. At this position, the beam becomes fully polarized and the prescribed higher-order polarization distribution emerges, while the field remains spatially partially coherent. Upon further propagation, the constituent modes lose their synchronization, the polarization purity decreases again, and the polarization information is transferred back into the two-point coherence structure. The occurrence of the deterministic polarization state is therefore localized around the designed propagation plane rather than maintained indefinitely.

For higher-order Poincaré-sphere states composed of two orthogonally polarized Laguerre–Gaussian modes, the distance z_c is independent of their topological charges, provided that both components undergo FrFTs of the same order. The two components then form their respective deterministic vortices in the same plane [93,94], where their spatial profiles and relative phases become synchronized. If different fractional orders are applied to the two polarization components, their deterministic vortices emerge at different distances. Their cross-spectral-density phases cannot then be simultaneously matched, and the resulting beam generally remains partially polarized while developing spatially

varying linear, elliptical, or spiral-like polarization distributions. The difference between the two fractional orders thus provides an additional degree of freedom for controlling polarization evolution.

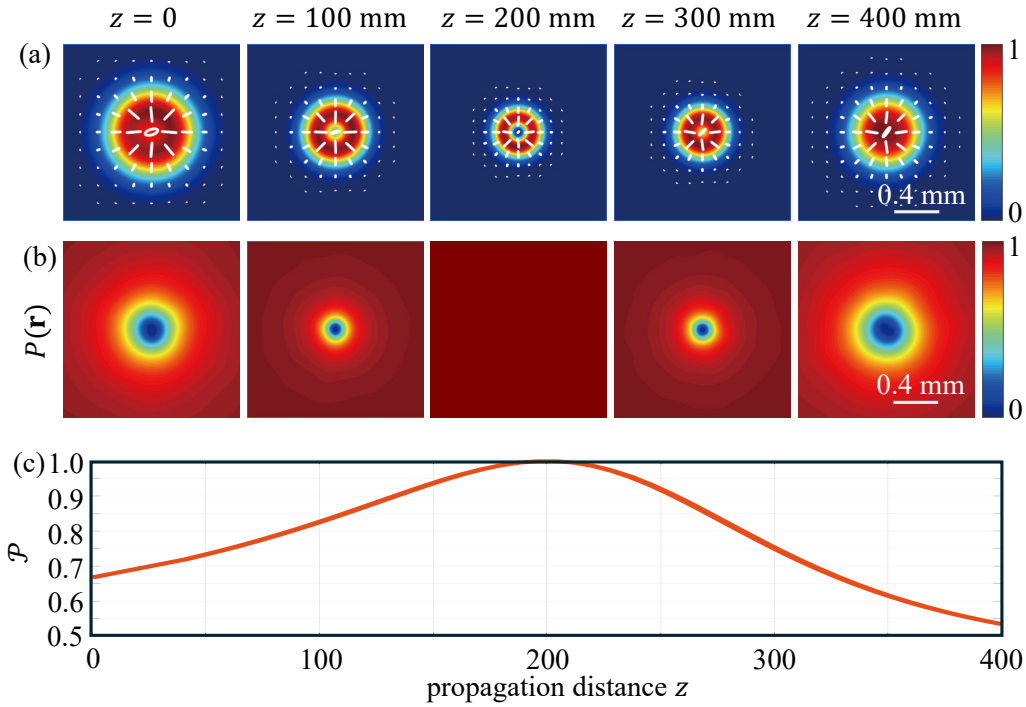


Figure 5. Propagation-dependent formation of a deterministic higher-order polarization state in a spatial-coherence-engineered vector beam. The beam is synthesized using a fractional Fourier-transform system and subsequently focused by a lens of focal length $f = 400$ mm. (**a**) Total intensity distributions and polarization ellipses of the fully polarized component at different propagation distances. (**b**) Corresponding spatial distributions of the local degree of polarization $P(\mathbf{r})$. (**c**) Evolution of the global polarization purity $\mathcal{P}$, defined as the power fraction carried by the fully polarized component. For the fractional order $p_E = 0.41$, the constituent modes become spatially and phase synchronized at the designed distance $z_c = 200$ mm. At this plane, the polarization purity reaches unity and the prescribed radial polarization state emerges. Further propagation breaks the modal synchronization, causing the local degree of polarization and global polarization purity to decrease again. From Ref. [92].

The higher-order polarization states reconstructed through Fourier-type coherence engineering exhibit strong robustness against atmospheric turbulence. This robustness relies on the separation of the source, detector, and turbulence time scales expressed by Equation (23). When $t_s \ll t_d \ll t_{turb}$, a large number of statistically independent source realizations pass through essentially the same frozen turbulence realization during a single detector exposure. The polarization matrix recorded at a given instant of the turbulent channel is therefore an average over many random source fields rather than over different turbulence realizations. This intrarealization averaging suppresses rapidly varying intensity and polarization fluctuations while preserving the coherence information used to reconstruct the target state.

The role of the spatial coherence width is illustrated in Figure 6. The left column shows representative random-field realizations in the source plane, while the right column presents the corresponding fields after propagation through strong atmospheric turbulence. As the spatial coherence width decreases from top to bottom, the characteristic speckle size of each realization becomes progressively smaller. Large speckles are strongly reshaped and displaced by turbulence, producing substantial deviations between the source and

received intensity distributions. By contrast, sufficiently small speckles experience a more nearly uniform phase perturbation over their individual spatial extent and are therefore less severely distorted. Their incoherent superposition consequently suppresses turbulence-induced fluctuations and allows the dark-hollow envelope associated with the encoded higher-order polarization state to remain discernible in the receiver plane.

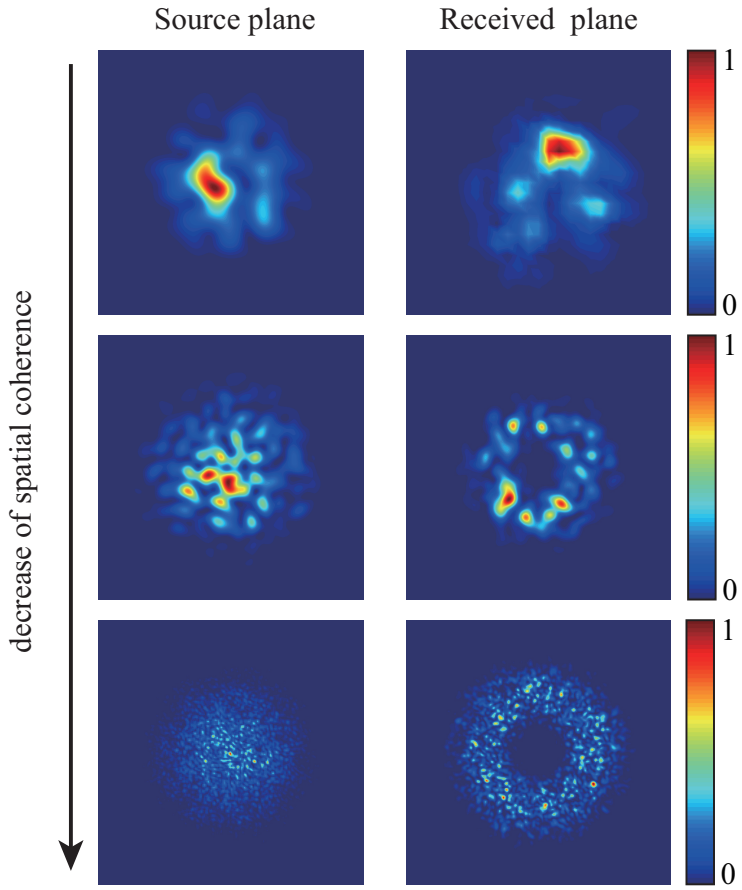


Figure 6. Representative normalized intensity distributions of random-field realizations associated with partially coherent sources of different spatial coherence widths. The left and right columns show the intensity distributions in the source and receiver planes, respectively, with the latter obtained after propagation through strong atmospheric turbulence. From top to bottom, the spatial coherence width decreases and the characteristic speckle size becomes progressively smaller. For sufficiently low spatial coherence, the turbulence-distorted field retains the dark-hollow envelope associated with the encoded higher-order polarization state, demonstrating the enhanced resilience of small-scale random modes to turbulent perturbations.

A smaller coherence width also increases the number of statistically independent random realizations. Averaging over these realizations reduces intensity scintillation, beam wander, and sensitivity to localized amplitude or phase perturbations. When the source coherence area is sufficiently smaller than the characteristic transverse scale of the turbulent distortion, the reconstructed polarization matrix is governed predominantly by the engineered coherence structure. The polarization information can therefore be recovered without estimating or inverting the instantaneous turbulent channel. Within the demonstrated family of higher-order polarization states, this protection mechanism is determined primarily by the source statistics and coherence width rather than by the particular polarization state being encoded.

6. Strategies for Spatial Coherence Engineering

The experimental strategies for tailoring spatial coherence, or equivalently for encoding a prescribed higher-order polarization state into the coherence structure of a partially coherent source, can be broadly divided into two categories. The first constructs a partially coherent source from a spatially incoherent primary source through a deterministic optical system, whereas the second directly synthesizes the partially coherent field by temporally superposing an ensemble of statistically designed coherent random modes.

The first strategy is based on the generalized van Cittert–Zernike theorem. Equation (28) can be rewritten as [66]

$$W_{\alpha\beta}(\mathbf{r}_1, \mathbf{r}_2) = \iint p_{\alpha\beta}(\mathbf{v}_1)\delta(\mathbf{v}_1 - \mathbf{v}_2)H^*_{\alpha}(\mathbf{r}_1, \mathbf{v}_1)H_{\beta}(\mathbf{r}_2, \mathbf{v}_2)\,\mathrm{d}^2\mathbf{v}_1\,\mathrm{d}^2\mathbf{v}_2, \tag{43}$$

where $\delta(\mathbf{v}_1 - \mathbf{v}_2)$ is the two-dimensional Dirac delta function. The quantity

$$W^{(\mathrm{in})}_{\alpha\beta}(\mathbf{v}_1, \mathbf{v}_2) = p_{\alpha\beta}(\mathbf{v}_1)\delta(\mathbf{v}_1 - \mathbf{v}_2) \tag{44}$$

may be interpreted as the cross-spectral density matrix of a spatially incoherent primary source whose local polarization matrix is $\mathbf{p}(\mathbf{v})$. After transmission through an optical system characterized by the polarization-dependent response functions $H_x(\mathbf{r}, \mathbf{v})$ and $H_y(\mathbf{r}, \mathbf{v})$, the one-point polarization information carried by $\mathbf{p}(\mathbf{v})$ is converted into the two-point coherence structure $\mathbf{W}(\mathbf{r}_1, \mathbf{r}_2)$ of the resulting partially coherent secondary source.

Experimentally, a spatially incoherent primary source with a prescribed polarization distribution can be produced by passing a fully coherent higher-order polarization-state beam through a rotating ground-glass disk (RGGD). If the RGGD is approximately isotropic and polarization independent, each point of the incident beam acquires the same random phase in its two orthogonal polarization components. The local polarization state is therefore preserved, whereas the spatial coherence is substantially reduced. When the illuminated area contains a sufficiently large number of statistically independent inhomogeneities of the RGGD, the transmitted field can be approximated as spatially delta-correlated [20,66].

A representative implementation is shown in Figure 7. Two Laguerre–Gaussian modes carrying orthogonal circular polarizations are first generated and coherently superposed with a Ronchi grating to form the desired fully coherent higher-order polarization state. The beam subsequently illuminates the RGGD, which converts it into a spatially incoherent vector source while preserving its local polarization distribution. A Fourier-transform system composed of a thin lens and an amplitude filter then produces the secondary partially coherent source. In this arrangement, the response functions $H_x(\mathbf{r}, \mathbf{v})$ and $H_y(\mathbf{r}, \mathbf{v})$ have the Fourier-transform form introduced in Equation (31); consequently, the polarization matrix of the primary source is encoded into the spatial coherence structure of the secondary source.

Figure 8a,b show the measured propagation characteristics of the resulting spatial-coherence-engineered beam. In the secondary-source plane, the prescribed higher-order polarization distribution is stored predominantly in the two-point coherence matrix and is largely obscured by an unpolarized background. As the beam approaches the focal plane, the encoded correlations are progressively converted into a one-point polarization distribution. The polarization texture becomes increasingly well defined between $z = 330$ mm and $z = 400$ mm, while the local degree of polarization increases simultaneously. At the focal plane, $z = 400$ mm, a dark-hollow intensity distribution and the prescribed higher-order polarization state are reconstructed with high polarization purity. As shown in Figure 8b, the degree of polarization approaches unity over most of the effective annular beam area, defined as the region in which the intensity exceeds 10% of its maximum value. The

reduced degree of polarization near the beam center has little influence on the recovered state because this region coincides with the low-intensity polarization singularity.

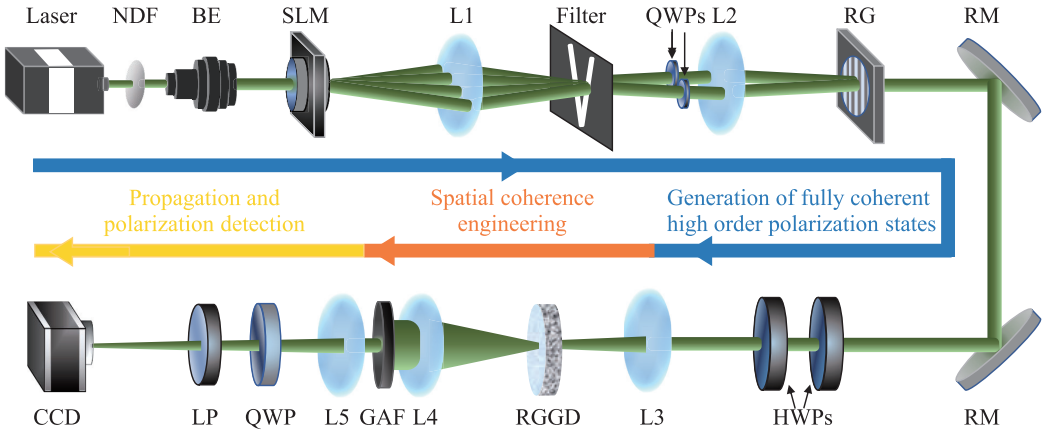


Figure 7. Experimental setup for generating a spatial-coherence-engineered vector beam using the generalized van Cittert–Zernike theorem. A linearly polarized laser beam is shaped by an SLM and a common-path $4f$ system composed of lenses L1 and L2. The selected ± 1 diffraction orders are converted by quarter-wave plates (QWPs) into orthogonally circularly polarized Laguerre–Gaussian modes with opposite topological charges and are subsequently combined by a Ronchi grating (RG) to form a fully coherent higher-order polarization state. Its polar and azimuthal parameters, Θ and Φ, are controlled by the modal intensity ratio and the half-wave plates (HWPs), respectively. Lens L3 focuses the beam onto a rotating ground-glass disk (RGGD), which reduces its spatial coherence while preserving the local polarization state. Lens L4 and a Gaussian amplitude filter (GAF) then generate the engineered partially coherent source. The propagation-dependent polarization properties are measured using lens L5, a QWP, a linear polarizer (LP), and a CCD camera. NDF, neutral-density filter; BE, beam expander; RM, reflecting mirror. From Ref. [66].

The robustness of this reconstruction against a dynamically varying channel is demonstrated in Figure 8c,d. After transmission through thermally induced turbulence generated by a graphite plate at 200 °C, the instantaneous x-polarized intensity of the engineered partially coherent beam retains the characteristic six-lobed distribution of the encoded higher-order polarization state over different measurement times. By contrast, the corresponding fully coherent beam undergoes pronounced deformation and displacement under the same turbulence. This difference originates from the rapid statistical fluctuations generated by the RGGD. The condition $t_s \ll t_d \ll t_{turb}$ is satisfied, so the detector averages over a large number of statistically independent source realizations while the turbulent channel remains approximately frozen. This intrarealization averaging suppresses turbulence-induced fluctuations and allows the higher-order polarization information encoded in the spatial coherence structure to be recovered without estimating or inverting the instantaneous turbulent channel.

The second strategy is based on the coherent-mode representation of partially coherent light. For a physically realizable cross-spectral density matrix, the vectorial Mercer expansion can be written as [50]

$$\mathbf{W}(\mathbf{r}_1, \mathbf{r}_2) = \sum_{m=1}^{\infty} \lambda_m \boldsymbol{\mathcal{E}}_m^*(\mathbf{r}_1) \boldsymbol{\mathcal{E}}_m^{\mathrm{T}}(\mathbf{r}_2), \qquad \lambda_m \geq 0, \tag{45}$$

where $\boldsymbol{\mathcal{E}}_m(\mathbf{r})$ are mutually orthonormal coherent vector modes and λ_m are the corresponding eigenvalues. The modes and their weights are obtained by solving the associated vectorial Fredholm integral equation. Although this representation provides a rigorous modal description, its direct implementation can be cumbersome because the eigenvalue problem generally has no simple analytical solution.

The orthogonality requirement can be relaxed by employing pseudo-mode or random-mode representations [95–99]. In the latter case, the cross-spectral density matrix is approximated through an ensemble average over M statistically independent, but not necessarily orthogonal, coherent vector fields:

$$\mathbf{W}(\mathbf{r}_1, \mathbf{r}_2) \simeq \frac{1}{M} \sum_{m=1}^{M} \boldsymbol{\mathcal{E}}_m^*(\mathbf{r}_1) \boldsymbol{\mathcal{E}}_m^{\mathrm{T}}(\mathbf{r}_2). \tag{46}$$

The common factor $1/M$ may alternatively be absorbed into the definitions of the modes or their weights. A sufficiently large value of M must be used for the finite ensemble to converge to the prescribed cross-spectral density matrix, and the required number of modes generally increases with the decrease in the spatial coherence width.

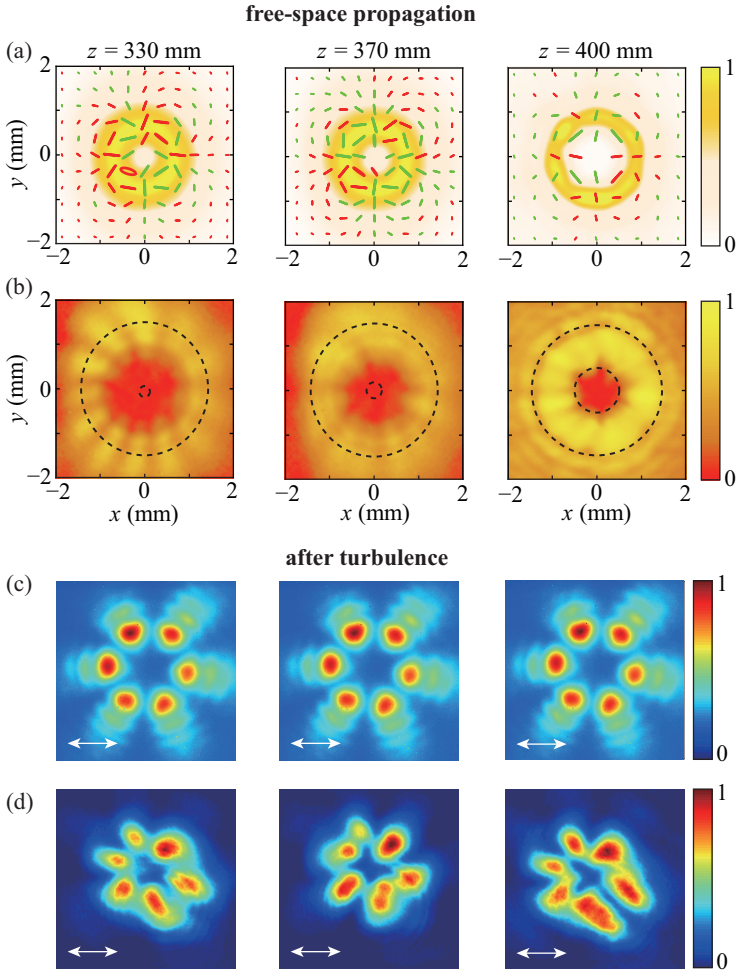


Figure 8. Experimental propagation and turbulence robustness of a spatial-coherence-engineered beam carrying an encoded higher-order polarization state. (**a**) Measured intensity and polarization distributions of the focused beam at $z = 330$, 370, and 400 mm, showing the progressive emergence of the encoded polarization state toward the focal plane. (**b**) Corresponding distributions of the local degree of polarization. The regions between the dashed contours indicate where the intensity exceeds 10% of its maximum value. (**c**) Representative instantaneous x-polarized intensity distributions of the engineered partially coherent beam after propagation through thermally induced turbulence generated by a graphite plate at 200 °C. (**d**) Corresponding results for the fully coherent higher-order polarization-state beam under the same turbulence. The partially coherent beam retains a stable six-lobed pattern, whereas the coherent beam undergoes pronounced turbulence-induced distortion. The white arrows in (**c**,**d**) denote the x-polarized intensity distributions. Adapted from Ref. [66].

For the Fourier-type coherence structure considered here, each random vector mode can be constructed as

$$\boldsymbol{\mathcal{E}}_m(\mathbf{r}) = T(\mathbf{r})\boldsymbol{\mathcal{R}}_m(\mathbf{r}), \tag{47}$$

where $T(\mathbf{r})$ determines the average source intensity envelope and

$$\boldsymbol{\mathcal{R}}_m(\mathbf{r}) = \int \mathbf{E}(\mathbf{v}) \frac{a_m(\mathbf{v}) + \mathrm{i}b_m(\mathbf{v})}{\sqrt{2}} \exp(-\mathrm{i}c_0\mathbf{r}\cdot\mathbf{v})\, \mathrm{d}^2\mathbf{v}. \tag{48}$$

Here, $\mathbf{E}(\mathbf{v})$ is the Jones field of the prescribed fully coherent higher-order polarization state, c_0 is a real parameter controlling the spatial coherence width, and $a_m(\mathbf{v})$ and $b_m(\mathbf{v})$ are independent realizations of zero-mean, unit-variance real Gaussian random processes. Their ideal correlations satisfy

$$\langle a_m(\mathbf{v}_1)a_n(\mathbf{v}_2)\rangle = \delta_{mn}\delta(\mathbf{v}_1 - \mathbf{v}_2), \tag{49}$$

$$\langle b_m(\mathbf{v}_1)b_n(\mathbf{v}_2)\rangle = \delta_{mn}\delta(\mathbf{v}_1 - \mathbf{v}_2), \tag{50}$$

$$\langle a_m(\mathbf{v}_1)b_n(\mathbf{v}_2)\rangle = 0. \tag{51}$$

Substitution of Equations (47) and (48) into Equation (46) reproduces the desired Schell-model cross-spectral density matrix in the limit of a sufficiently large ensemble. The target higher-order polarization state is determined by $\mathbf{E}(\mathbf{v})$, whereas c_0, the spatial extent of $\mathbf{E}(\mathbf{v})$, and the source envelope $T(\mathbf{r})$ control the coherence width and average intensity profile.

Equation (48) also clarifies the correspondence between the two engineering strategies. The factor $[a_m(\mathbf{v}) + \mathrm{i}b_m(\mathbf{v})]/\sqrt{2}$ numerically emulates an instantaneous complex transmission function of the RGGD, the Fourier kernel represents propagation through the Fourier-transform system, and $T(\mathbf{r})$ plays the role of the amplitude filter. Random-mode synthesis therefore replaces the rotating diffuser and the subsequent coherence-forming optics with digitally generated field realizations. More general propagation kernels may also be incorporated into the calculated random modes, substantially extending the range of realizable correlation structures without requiring a dedicated physical optical system for every kernel.

The random modes can be generated experimentally by sequentially displaying time-varying multiplexed computer-generated holograms (CGHs) on a spatial light modulator [98]. As shown in Figure 9, the two scalar components of each random vector mode are encoded into separate regions or diffraction directions of a multiplexed CGH. Their selected first diffraction orders are spatially filtered, transformed into two orthogonal polarization states, and recombined with a Ronchi grating in a common-path interferometric system. Sequential display of M statistically independent CGHs, followed by temporal integration at the detector, produces the prescribed partially coherent vector source.

Figure 10 shows the measured intensity, polarization distribution, and degree of polarization of the synthesized beam during propagation. The individual random modes contain speckled intensity distributions and spatially random polarization states, while their time-averaged source has a smooth Gaussian intensity profile and may be nearly unpolarized. As the propagation distance increases, the average intensity evolves from a Gaussian to a dark-hollow distribution, the degree of polarization increases, and the higher-order polarization state encoded in the coherence structure gradually becomes visible. In the focal plane, the beam is effectively fully polarized over its high-intensity region and reproduces the encoded higher-order polarization state. Compared with the RGGD-based implementation, digital random-mode synthesis is more compact and flexible, and it permits direct adjustment of the encoded polarization state, source profile, and coherence width through the calculated holograms.

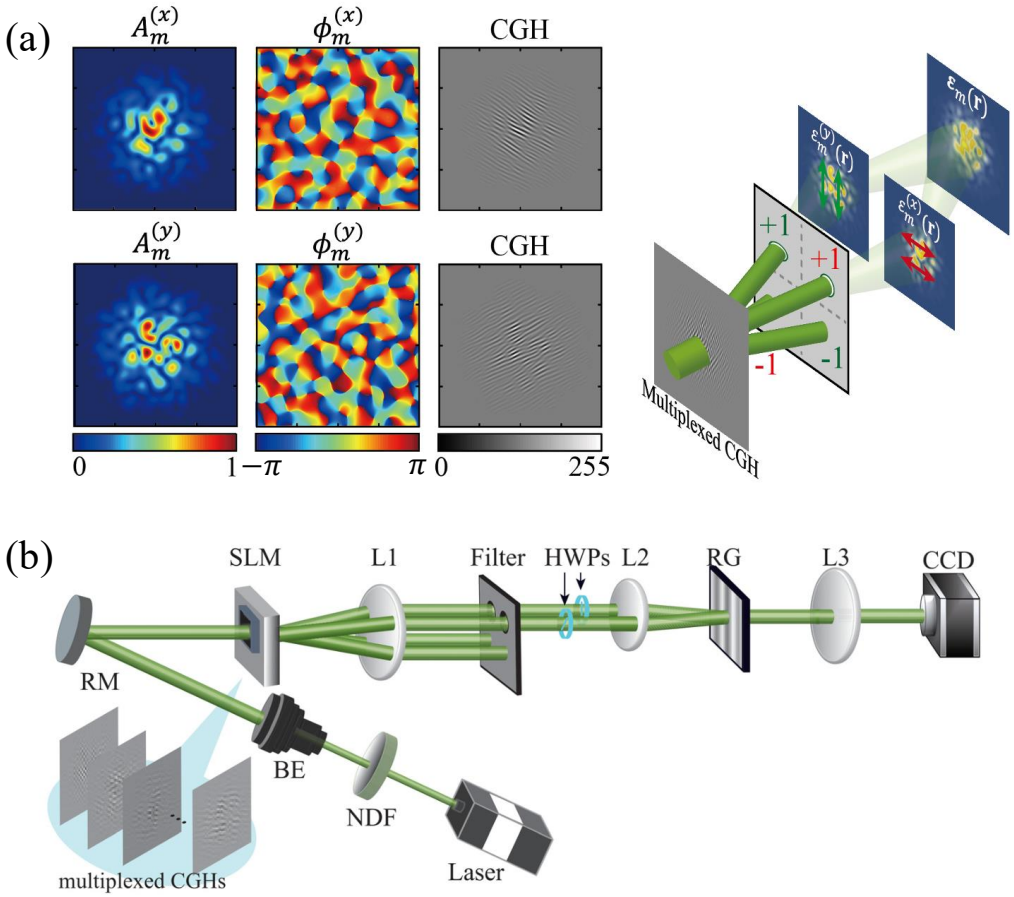


Figure 9. Random-mode synthesis of a spatial-coherence-engineered vector beam. (**a**) Construction of a single random vector mode using a multiplexed computer-generated hologram (CGH). The prescribed amplitudes $A_m^{(x)}(\mathbf{r})$ and $A_m^{(y)}(\mathbf{r})$ and phases $\phi_m^{(x)}(\mathbf{r})$ and $\phi_m^{(y)}(\mathbf{r})$ of the two scalar components are encoded into separate CGHs and combined into a single multiplexed hologram. The corresponding $+1$ diffraction orders are spatially filtered, converted into orthogonal linear polarization states, and coherently superposed to produce the random vector mode $\boldsymbol{\mathcal{E}}_m(\mathbf{r})$. (**b**) Experimental setup for synthesizing the partially coherent vector source. A sequence of time-varying multiplexed CGHs is displayed on the SLM to generate statistically independent random modes. Lenses L1 and L2 form a common-path $4f$ system, in which a spatial filter selects the desired diffraction orders, half-wave plates (HWPs) establish orthogonal polarizations, and a Ronchi grating (RG) recombines the two components. Temporal averaging over the generated modes produces the prescribed spatial-coherence-engineered beam, whose propagation characteristics are measured using lens L3 and a CCD camera. NDF, neutral-density filter; BE, beam expander; RM, reflecting mirror. Adapted from Ref. [98].

A practical limitation of liquid-crystal SLMs is their relatively low refresh rate, which is typically on the order of 60 Hz. The resulting source fluctuation time t_s is then comparable to the characteristic time of many laboratory or atmospheric turbulence channels. Moreover, a detector must integrate over a sufficiently large number of random modes to reproduce the prescribed ensemble statistics. It can therefore be difficult to simultaneously satisfy $t_s \ll t_d \ll t_{turb}$, which is required for intrarealization averaging within an approximately frozen turbulent channel.

Faster random-mode synthesis can be achieved using a digital micromirror device (DMD) [100,101]. Unlike a liquid-crystal SLM, which primarily provides phase modulation through electrically controlled birefringence, a DMD consists of an array of binary tilting micromirrors and acts as a high-speed amplitude modulator. A grayscale complex-amplitude CGH can be converted into a binary hologram using the Floyd–Steinberg error-diffusion al-

gorithm. The DMD itself remains an amplitude-only device; the prescribed complex field is reconstructed in a selected diffraction order after spatial filtering. By dividing a single DMD into two regions and combining the reconstructed fields in a common-path interferometer, the two orthogonal components of a random vector mode can be modulated synchronously, which is essential for accurately controlling their complex cross-correlation [102]. The DMD used in the reported implementation operated at a refresh rate of approximately 17 kHz. Such high-speed modulation substantially reduces t_s and makes the temporal hierarchy required for turbulence-resistant synthesis more accessible.

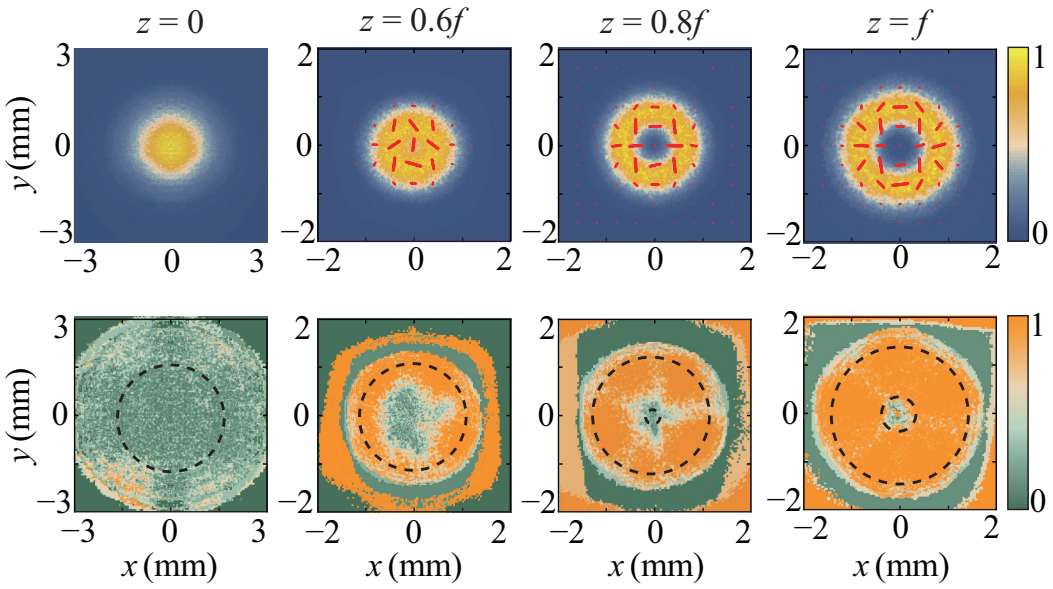


Figure 10. Measured propagation characteristics of the spatial-coherence-engineered vector beam synthesized by random-mode superposition. The upper row shows the normalized intensity distributions and the polarization ellipses of the fully polarized component at $z = 0, 0.6f, 0.8f$, and f. The lower row presents the corresponding local degree of polarization $P(\mathbf{r})$; the dashed contours delimit the effective beam region in which the intensity exceeds 10% of its maximum value. The source is initially almost unpolarized, with the prescribed higher-order polarization state encoded in its two-point coherence structure. During propagation, the degree of polarization increases and the encoded polarization texture gradually emerges. In the focal plane, the beam forms a dark-hollow intensity distribution and becomes effectively fully polarized throughout most of the high-intensity annular region. From Ref. [98].

Electro-optic modulators provide a further route toward higher-speed spatial coherence engineering. A recently demonstrated lithium-niobate-film modulator used 64 independently driven one-dimensional channels to synthesize prescribed phase realizations through the Pockels effect. The device achieved a binary modulation rate of 2 MHz and an experimental 0–2π phase-modulation rate of 350 kHz, approximately twenty times higher than previously reported spatial-coherence modulation rates [103]. This experiment demonstrated the synthesis of one-dimensional scalar Gaussian Schell-model sources using 625 coherent modes and verified the resulting coherence through Young's interference measurements. Although vectorial higher-order polarization-state encoding and two-dimensional coherence control have not yet been demonstrated with this device, extension to two-dimensional electrode arrays and synchronized polarization channels could provide a promising platform for ultrafast synthesis of turbulence-resistant partially coherent vector beams.

The two classes of spatial coherence engineering are therefore complementary. The incoherent-source approach is conceptually direct, naturally provides rapid statistical fluctuations, and has already demonstrated robust higher-order polarization-state recon-

struction through atmospheric turbulence, although its programmability is limited by the employed optical system. Digital random-mode synthesis offers substantially greater control over the intensity, phase, polarization, and correlation functions, but its performance in dynamic channels depends critically on the modulation rate. Liquid-crystal SLMs provide flexible phase modulation and high spatial resolution but typically operate at only tens of hertz. DMDs achieve kilohertz to tens-of-kilohertz modulation rates, although their binary-amplitude operation requires additional holographic encoding. Lithium-niobate electro-optic modulators can further increase the modulation rate from hundreds of kilohertz to several megahertz, enabling coherence engineering in more rapidly varying channels, but generally at the cost of greater device and system complexity. These platforms therefore involve a trade-off among modulation flexibility, speed, spatial resolution, and experimental complexity. The development from liquid-crystal SLMs to DMDs and lithium-niobate electro-optic modulators represents a progression toward flexible, high-speed, and eventually real-time synthesis of robust higher-order polarization states.

7. Conclusions and Discussion

This review has examined the robust synthesis of higher-order polarization states through partial-coherence engineering. Unlike conventional approaches in which the target polarization texture is directly carried by a coherent field, this strategy encodes the prescribed polarization matrix into the two-point coherence structure of a partially coherent vector source. Propagation subsequently converts the engineered coherence structure into a directly observable polarization distribution, enabling the target state to emerge in the far field, a focal plane, or a prescribed finite propagation plane.

The spatial and temporal diversity of partially coherent light can suppress the effect of turbulence when the source coherence width, detector integration time, and channel dynamics are appropriately matched. Experimental implementations based on RGGDs, SLMs, and DMDs have demonstrated the feasibility and robustness of this concept, while recent electro-optic modulation techniques offer a route toward substantially higher operating speeds. These developments establish spatial coherence as an active degree of freedom for storing, transporting, and reconstructing structured polarization information.

Despite this progress, several conceptual and practical challenges remain. First, most existing demonstrations are based on idealized propagation conditions. The atmosphere is commonly represented as a paraxial, polarization-independent phase channel with Kolmogorov or von Kármán statistics. Practical links may additionally involve finite apertures, absorption, anisotropy, birefringence, polarization-dependent loss, non-Kolmogorov fluctuations, chromatic dispersion, strong scintillation, and multiple scattering. These effects can render the effective channel nonunitary or couple both the spatial and polarization degrees of freedom. The performance of coherence-encoded polarization states under such conditions, particularly over long outdoor propagation paths and with limited receiver apertures, remains to be systematically investigated.

Second, the robustness mechanism imposes a demanding temporal condition. The detector must satisfy $t_s \ll t_d \ll t_{turb}$ so that it averages over many source realizations while the turbulent channel remains approximately frozen. RGGD-based methods naturally provide short source coherence times but offer limited programmability and relatively low optical efficiency. Liquid-crystal SLMs provide flexible field control but generally operate too slowly for rapidly varying channels. DMDs offer kilohertz modulation but are limited by binary-amplitude encoding, diffraction efficiency, and spatial bandwidth. Lithium-niobate electro-optic modulators can operate at much higher rates, although current demonstrations are restricted mainly to one-dimensional scalar coherence control.

Developing two-dimensional, high-resolution vectorial modulators with synchronized polarization channels is therefore a central technological objective.

The spatial coherence width must also be optimized rather than simply minimized. Reducing the coherence width increases the number of independently fluctuating spatial modes and generally improves resistance to localized perturbations. Excessively low coherence, however, can increase beam divergence, reduce the collected power, broaden the reconstructed features, and impose higher requirements on the number and speed of the generated random modes. A practical system must therefore balance turbulence robustness against propagation loss, receiver aperture, spatial resolution, polarization purity, and statistical convergence. Establishing quantitative design rules for this tradeoff will be important for translating laboratory demonstrations into real optical links.

Future source design may benefit from combining partial-coherence engineering with adaptive and computational techniques. Partial coherence can provide passive, high-speed statistical stabilization, while adaptive optics compensates slowly varying low-order aberrations. Transmission eigenmodes may be used to optimize the average transfer efficiency, whereas error-correcting codes can protect the information encoded in the recovered polarization states. Data-driven optimization could further identify weighting matrices, kernel functions, and random-mode ensembles that maximize a task-specific performance metric under measured channel statistics. Such hybrid approaches may outperform methods based exclusively on either passive robustness or active channel correction.

The measurement of complex coherence structures is another important challenge. Conventional coherence measurements often require multiple sequential intensity acquisitions [104–109], which limits their use in dynamic environments. Single-shot, multiplexed, or high-speed tomography methods capable of recovering all complex correlation functions would enable real-time monitoring of the encoded information and provide feedback for adaptive source optimization.

These developments may support a broad range of applications. In free-space optical communication, several higher-order polarization states could be multiplexed into distinct coherence channels to improve channel capacity, security, and resilience to turbulence [110,111]. In imaging and remote sensing, coherence-engineered illumination may suppress speckle while preserving polarization-sensitive contrast through random media [112–114]. In optical encryption, information can be hidden in complex correlation functions that are inaccessible through direct intensity measurements [115,116]. Robust polarization textures may also improve optical trapping, particle transport, micromanipulation, laser processing, and the delivery of structured angular momentum through disturbed environments.

Overall, partial-coherence engineering offers a promising route from fragile coherent polarization structures to statistically robust vector fields. Its future development will depend on advances in high-speed multidimensional modulation, complete coherence measurement, realistic channel modeling, and application-oriented optimization. Progress in these areas should enable robust higher-order polarization states to move from proof-of-principle experiments toward practical communication, sensing, imaging, and light-manipulation systems.

Author Contributions: Conceptualization, Y.C. (Yahong Chen); validation, Y.S., Y.Z., X.Y., Z.H., J.S., F.W., Y.C. (Yangjian Cai), and Y.C. (Yahong Chen); formal analysis, Y.S., Y.Z., X.Y., and Y.C. (Yahong Chen); resources, Y.C. (Yahong Chen); writing—original draft preparation, Y.S., Y.Z., X.Y., and Y.C. (Yahong Chen); writing—review and editing, Y.C. (Yahong Chen); visualization, Y.S., Y.Z., X.Y., Z.H., J.S., F.W., Y.C. (Yangjian Cai), and Y.C. (Yahong Chen); supervision, Y.C. (Yahong Chen); project administration, F.W., Y.C. (Yangjian Cai), and Y.C. (Yahong Chen); funding acquisition, F.W., Y.C.

(Yangjian Cai), and Y.C. (Yahong Chen). All authors have read and agreed to the published version of the manuscript.

Funding: This research was funded by the National Key Research and Development Program of China (Grant No. 2022YFA1404800), the National Natural Science Foundation of China (Grants No. 12274310, No. 12274311), Postgraduate Research & Practice Innovation Program of Jiangsu Province (Grant No. 26CXJH5832), Hui-Chun Chin and Tsung-Dao Lee Chinese Undergraduate Research Endowment (CURE) (Yue Sun), and the Undergraduate Training Program for Innovation and Entrepreneurship, Soochow University (Yin Zhang and Xudong Yan).

Institutional Review Board Statement: Not applicable.

Informed Consent Statement: Not applicable.

Data Availability Statement: All data needed to evaluate the conclusions in the paper are present in the paper.

Conflicts of Interest: The authors declare no conflicts of interest.

Abbreviations

The following abbreviations are used in this manuscript:

HOPS	Higher-order Poincaré-sphere
FrFT	Fractional Fourier transform
RGGD	Rotating ground-glass disk
SLM	Spatial light modulator
QWP	Quarter-wave plate
RG	Ronchi grating
HWP	Half-wave plate
GAF	Gaussian amplitude filter
NDF	Neutral-density filter
BE	Beam expander
RM	Reflecting mirror
CGH	Computer-generated hologram
DMD	Digital micromirror device

References

1. Goldstein, D.H. *Polarized Light*, 3rd ed.; CRC Press: Boca Raton, FL, USA, 2017.
2. Brosseau, C. *Fundamentals of Polarized Light: A Statistical Optics Approach*; Wiley: New York, NY, USA, 1998.
3. Gil, J.J.; Ossikovski, R. *Polarized Light and the Mueller Matrix Approach*; CRC Press: Boca Raton, FL, USA, 2022.
4. Chekhova, M.; Banzer, P. *Polarization of Light: In Classical, Quantum, and Nonlinear Optics*; De Gruyter: Berlin, Germany, 2021.
5. Zhan, Q. Cylindrical vector beams: From mathematical concepts to applications. *Adv. Opt. Photonics* **2009**, *1*, 1–57. [CrossRef]
6. Fu, S.; Gao, C. Vector beams and vectorial vortex beams. In *Optical Vortex Beams: Fundamentals and Techniques*; Springer Nature: Singapore, 2023; pp. 277–333.
7. Forbes, A.; de Oliveira, M.; Dennis, M.R. Structured light. *Nat. Photonics* **2021**, *15*, 253–262. [CrossRef]
8. Rubinsztein-Dunlop, H.; Forbes, A.; Berry, M.V.; Dennis, M.R.; Andrews, D.L.; Mansuripur, M.; Denz, C.; Alpmann, C.; Banzer, P.; Bauer, T.; et al. Roadmap on structured light. *J. Opt.* **2017**, *19*, 013001. [CrossRef]
9. He, C.; Shen, Y.; Forbes, A. Towards higher-dimensional structured light. *Light Sci. Appl.* **2022**, *11*, 205. [CrossRef] [PubMed]
10. Zhen, W.; Wang, X.-L.; Ding, J.; Wang, H.-T. Controlling the symmetry of the photonic spin Hall effect by an optical vortex pair. *Phys. Rev. A* **2023**, *108*, 023514. [CrossRef]
11. Zhen, W.; Wang, X.-L.; Ding, J.; Wang, H.-T. Revisiting physical mechanism of longitudinal photonic spin splitting and Goos–Hänchen shift. *New J. Phys.* **2024**, *26*, 013045. [CrossRef]
12. Zhen, W.; Ren, Z.-C.; Wang, X.-L.; Ding, J.; Wang, H.-T. Polarization structure transition of C-point singularities upon reflection. *Sci. China Phys. Mech. Astron.* **2025**, *68*, 244211. [CrossRef]
13. Zhen, W.; Qing, Z.; Yan, W.; Ren, Z.-C.; Wang, X.-L.; Wang, H.-T.; Ding, J.; Shen, Y. Reconfiguring optical skyrmion topology in free space. *Optica* **2026**, *13*, 188–194. [CrossRef]

14. Rosales-Guzmán, C.; Ndagano, B.; Forbes, A. A review of complex vector light fields and their applications. *J. Opt.* **2018**, *20*, 123001. [CrossRef]
15. Milione, G.; Sztul, H.I.; Nolan, D.A.; Alfano, R.R. Higher-order Poincaré sphere, Stokes parameters, and the angular momentum of light. *Phys. Rev. Lett.* **2011**, *107*, 053601. [CrossRef] [PubMed]
16. Nape, I.; Singh, K.; Klug, A.; Buono, W.; Rosales-Guzmán, C.; McWilliam, A.; Franke-Arnold, S.; Kritzinger, A.; Forbes, P.; Dudley, A.; et al. Revealing the invariance of vectorial structured light in complex media. *Nat. Photonics* **2022**, *16*, 538–546. [CrossRef]
17. Peters, C.; Cox, M.; Drozdov, A.; Forbes, A. The invariance and distortion of vectorial light across a real-world free-space link. *Appl. Phys. Lett.* **2023**, *123*, 021103. [CrossRef]
18. Singh, K.; Nape, I.; Buono, W.T.; Dudley, A.; Forbes, A. A robust basis for multi-bit optical communication with vectorial light. *Laser Photonics Rev.* **2023**, *17*, 2200844. [CrossRef]
19. Wang, J.; Svensson, S.J.; Clark, T.W.; Chen, Y.; Al Khafaji, M.A.; Gao, H.; Westerberg, N.; Franke-Arnold, S. Measuring the optical concurrence of vector beams with an atomic-state interferometer. *Phys. Rev. Lett.* **2024**, *132*, 193803. [CrossRef] [PubMed]
20. Hu, Z.; Shen, J.; Zhu, Y.; Liu, Y.; Liu, L.; Friberg, A.T.; Setälä, T.; Cai, Y.; Wang, F.; Chen, Y. Robust measurement of the concurrence of vector light beams. *Phys. Rev. Lett.* **2025**, *135*, 253801. [CrossRef] [PubMed]
21. Milione, G.; Nguyen, T.A.; Leach, J.; Nolan, D.A.; Alfano, R.R. Using the nonseparability of vector beams to encode information for optical communication. *Opt. Lett.* **2015**, *40*, 4887–4890. [CrossRef] [PubMed]
22. Willner, A.E. Vector-mode multiplexing brings an additional approach for capacity growth in optical fibers. *Light Sci. Appl.* **2018**, *7*, 18002. [CrossRef] [PubMed]
23. Berg-Johansen, S.; Töppel, F.; Stiller, B.; Banzer, P.; Ornigotti, M.; Giacobino, E.; Leuchs, G.; Aiello, A.; Marquardt, C. Classically entangled optical beams for high-speed kinematic sensing. *Optica* **2015**, *2*, 864–868. [CrossRef]
24. Fang, L.; Wan, Z.; Forbes, A.; Wang, J. Vectorial Doppler metrology. *Nat. Commun.* **2021**, *12*, 4186. [CrossRef] [PubMed]
25. Ndagano, B.; Perez-Garcia, B.; Roux, F.S.; McLaren, M.; Rosales-Guzmán, C.; Zhang, Y.; Mouane, O.; Hernandez-Aranda, R.I.; Konrad, T.; Forbes, A. Characterizing quantum channels with non-separable states of classical light. *Nat. Phys.* **2017**, *13*, 397–402. [CrossRef]
26. Sit, A.; Bouchard, F.; Fickler, R.; Gagnon-Bischoff, J.; Larocque, H.; Heshami, K.; Elser, D.; Peuntinger, C.; Günthner, K.; Heim, B.; et al. High-dimensional intracity quantum cryptography with structured photons. *Optica* **2017**, *4*, 1006–1010. [CrossRef]
27. Forbes, A.; Nape, I. Quantum mechanics with patterns of light: Progress in high-dimensional and multidimensional entanglement with structured light. *AVS Quantum Sci.* **2019**, *1*, 011701. [CrossRef]
28. Djordjevic, I.B.; Nafria, V. Classical coherent states based quantum information processing and quantum computing analogs. *IEEE Access* **2024**, *12*, 33569–33588. [CrossRef]
29. Meyer, J.; Reches, Y.; Rozenman, G.G.; Oz, Y.; Suchowski, H.; Arie, A. Analogy of free-space quantum key distribution using spatial modes of light: Scaling up the distance and the dimensionality. *Opt. Lett.* **2025**, *50*, 3297–3300. [CrossRef]
30. Cardano, F.; Karimi, E.; Slussarenko, S.; Marrucci, L.; De Lisio, C.; Santamato, E. Polarization pattern of vector vortex beams generated by q-plates with different topological charges. *Appl. Opt.* **2012**, *51*, C1–C6. [CrossRef] [PubMed]
31. Cardano, F.; Karimi, E.; Marrucci, L.; De Lisio, C.; Santamato, E. Generation and dynamics of optical beams with polarization singularities. *Opt. Express* **2013**, *21*, 8815–8820. [CrossRef] [PubMed]
32. Chen, S.; Zhou, X.; Liu, Y.; Ling, X.; Luo, H.; Wen, S. Generation of arbitrary cylindrical vector beams on the higher-order Poincaré sphere. *Opt. Lett.* **2014**, *39*, 5274–5276. [CrossRef] [PubMed]
33. Naidoo, D.; Roux, F.; Dudley, A.; Litvin, I.; Piccirillo, B.; Marrucci, L.; Forbes, A. Controlled generation of higher-order Poincaré sphere beams from a laser. *Nat. Photonics* **2016**, *10*, 327–332. [CrossRef]
34. Liu, Z.; Liu, Y.; Ke, Y.; Liu, Y.; Shu, W.; Luo, H.; Wen, S. Generation of arbitrary vector vortex beams on hybrid-order Poincaré sphere. *Photonics Res.* **2017**, *5*, 15–21. [CrossRef]
35. Devlin, R.C.; Ambrosio, A.; Rubin, N.A.; Mueller, J.P.B.; Capasso, F. Arbitrary spin-to-orbital angular momentum conversion of light. *Science* **2017**, *358*, 896–901. [CrossRef] [PubMed]
36. Otte, E.; Nape, I.; Rosales-Guzmán, C.; Vallés, A.; Denz, C.; Forbes, A. Recovery of nonseparability in self-healing vector Bessel beams. *Phys. Rev. A* **2018**, *98*, 053818. [CrossRef]
37. Wu, G.; Wang, F.; Cai, Y. Generation and self-healing of a radially polarized Bessel–Gauss beam. *Phys. Rev. A* **2014**, *89*, 043807. [CrossRef]
38. Cai, Y.; Lin, Q.; Eyyuboğlu, H.T.; Baykal, Y. Average irradiance and polarization properties of a radially or azimuthally polarized beam in a turbulent atmosphere. *Opt. Express* **2008**, *16*, 7665–7673. [CrossRef] [PubMed]
39. Cheng, W.; Haus, J.W.; Zhan, Q. Propagation of vector vortex beams through a turbulent atmosphere. *Opt. Express* **2009**, *17*, 17829–17836. [CrossRef] [PubMed]
40. Gu, Y.; Korotkova, O.; Gbur, G. Scintillation of nonuniformly polarized beams in atmospheric turbulence. *Opt. Lett.* **2009**, *34*, 2261–2263. [CrossRef] [PubMed]

41. Wei, C.; Wu, D.; Liang, C.; Wang, F.; Cai, Y. Experimental verification of significant reduction of turbulence-induced scintillation in a full Poincaré beam. *Opt. Express* **2015**, *23*, 24331–24341. [CrossRef] [PubMed]
42. Cox, M.A.; Mphuthi, N.; Nape, I.; Mashaba, N.; Cheng, L.; Forbes, A. Structured light in turbulence. *IEEE J. Sel. Top. Quantum Electron.* **2021**, *27*, 7500521. [CrossRef]
43. Peters, C.; Cocotos, V.; Forbes, A. Structured light in atmospheric turbulence—A guide to its digital implementation: Tutorial. *Adv. Opt. Photonics* **2025**, *17*, 113–184. [CrossRef]
44. Chen, J.; Kong, L.; Zhan, Q. Demonstration of a vectorial optical field generator with adaptive closed-loop control. *Rev. Sci. Instrum.* **2017**, *88*, 125111. [CrossRef] [PubMed]
45. Dai, Y.; He, C.; Wang, J.; Turcotte, R.; Fish, L.; Wincott, M.; Hu, Q.; Booth, M.J. Active compensation of extrinsic polarization errors using adaptive optics. *Opt. Express* **2019**, *27*, 35797–35811. [CrossRef] [PubMed]
46. Zhai, Y.; Fu, S.; Zhang, J.; Liu, X.; Zhou, H.; Gao, C. Turbulence aberration correction for vector vortex beams using deep neural networks on experimental data. *Opt. Express* **2020**, *28*, 7515–7527. [CrossRef] [PubMed]
47. Zhu, Z.; Janasik, M.; Fyffe, A.; Hay, D.; Zhou, Y.; Kantor, B.; Winder, T.; Boyd, R.W.; Leuchs, G.; Shi, Z. Compensation-free high-dimensional free-space optical communication using turbulence-resilient vector beams. *Nat. Commun.* **2021**, *12*, 1666. [CrossRef] [PubMed]
48. Klug, A.; Peters, C.; Forbes, A. Robust structured light in atmospheric turbulence. *Adv. Photonics* **2023**, *5*, 016006. [CrossRef]
49. Lu, X.; Wang, Z.; Zhan, Q.; Cai, Y.; Zhao, C. Coherence entropy during propagation through complex media. *Adv. Photonics* **2024**, *6*, 046002. [CrossRef]
50. Mandel, L.; Wolf, E. *Optical Coherence and Quantum Optics*; Cambridge University Press: Cambridge, UK, 1995.
51. Wolf, E. *Introduction to the Theory of Coherence and Polarization of Light*; Cambridge University Press: Cambridge, UK, 2007.
52. Goodman, J.W. *Statistical Optics*; Wiley: New York, NY, USA, 1985.
53. Ostrovsky, A.S. *Coherent-Mode Representations in Optics*; SPIE Press: Bellingham, WA, USA, 2006.
54. Shirai, T.; Dogariu, A.; Wolf, E. Mode analysis of spreading of partially coherent beams propagating through atmospheric turbulence. *J. Opt. Soc. Am. A* **2003**, *20*, 1094–1102. [CrossRef] [PubMed]
55. Gbur, G. Partially coherent beam propagation in atmospheric turbulence. *J. Opt. Soc. Am. A* **2014**, *31*, 2038–2045. [CrossRef] [PubMed]
56. Wang, F.; Liu, X.; Cai, Y. Propagation of partially coherent beams in turbulent atmosphere: A review. *Prog. Electromagn. Res.* **2015**, *150*, 123–143. [CrossRef]
57. Wu, G.; Wang, F.; Cai, Y. Coherence and polarization properties of a radially polarized beam with variable spatial coherence. *Opt. Express* **2012**, *20*, 28301–28318. [CrossRef] [PubMed]
58. Wang, F.; Liu, X.; Liu, L.; Yuan, Y.; Cai, Y. Experimental study of the scintillation index of a radially polarized beam with controllable spatial coherence. *Appl. Phys. Lett.* **2013**, *103*, 091102. [CrossRef]
59. Yu, J.; Huang, Y.; Wang, F.; Liu, X.; Gbur, G.; Cai, Y. Scintillation properties of a partially coherent vector beam with vortex phase in turbulent atmosphere. *Opt. Express* **2019**, *27*, 26676–26688. [CrossRef] [PubMed]
60. Wang, Y.; Gu, K.; Dong, Z.; Wang, F.; Chen, Y.; Cai, Y.; Liu, Y. Generation of partially coherent full Poincaré beam arrays and their Stokes scintillations in turbulent media. *Appl. Phys. Lett.* **2024**, *125*, 171102. [CrossRef]
61. Cai, Y.; Chen, Y.; Wang, F. Generation and propagation of partially coherent beams with nonconventional correlation functions: A review. *J. Opt. Soc. Am. A* **2014**, *31*, 2083–2096. [CrossRef] [PubMed]
62. Chen, Y.; Wang, F.; Cai, Y. Partially coherent light beam shaping via complex spatial coherence structure engineering. *Adv. Phys. X* **2022**, *7*, 2009742. [CrossRef]
63. Yu, J.; Zhu, X.; Wang, F.; Chen, Y.; Cai, Y. Research progress on manipulating spatial coherence structure of light beams and its applications. *Prog. Quantum Electron.* **2023**, *91*, 100486. [CrossRef]
64. Chen, Y.; Wang, F.; Liu, L.; Zhao, C.; Cai, Y.; Korotkova, O. Generation and propagation of a partially coherent vector beam with special correlation functions. *Phys. Rev. A* **2014**, *89*, 013801. [CrossRef]
65. Wang, F.; Chen, Y.; Liu, X.; Cai, Y.; Ponomarenko, S.A. Self-reconstruction of partially coherent light beams scattered by opaque obstacles. *Opt. Express* **2016**, *24*, 23735–23746. [CrossRef] [PubMed]
66. Dong, Z.; Chen, Y.; Wang, F.; Cai, Y.; Friberg, A.T.; Setälä, T. Encoding higher-order polarization states into robust partially coherent optical beams. *Phys. Rev. Appl.* **2022**, *18*, 034036. [CrossRef]
67. Yuan, B.; Dong, Z.; Liu, Y.; Wang, F.; Cai, Y.; Chen, Y. Robust high-order polarization arrays via vectorial spatial-coherence engineering. *Phys. Rev. Appl.* **2023**, *20*, 054031. [CrossRef]
68. Liu, Y.; Dong, Z.; Wang, F.; Cai, Y.; Chen, Y. Experimental synthesis of higher-order Poincaré sphere beam array with spatial coherence engineering. *Appl. Phys. Lett.* **2023**, *122*, 161106. [CrossRef]
69. Liu, Y.; Dong, Z.; Wang, F.; Chen, Y.; Cai, Y. Generation of a higher-order Poincaré sphere beam array with spatial coherence engineering. *Opt. Lett.* **2022**, *47*, 5220–5223. [CrossRef] [PubMed]
70. Forbes, A.; Aiello, A.; Ndagano, B. Classically entangled light. *Prog. Opt.* **2019**, *64*, 99–153. [CrossRef]

71. Wootters, W.K. Entanglement of formation of an arbitrary state of two qubits. *Phys. Rev. Lett.* **1998**, *80*, 2245–2248. [CrossRef]
72. Walborn, S.P.; Souto Ribeiro, P.H.; Davidovich, L.; Mintert, F.; Buchleitner, A. Experimental determination of entanglement with a single measurement. *Nature* **2006**, *440*, 1022–1024. [CrossRef] [PubMed]
73. McLaren, M.; Konrad, T.; Forbes, A. Measuring the nonseparability of vector vortex beams. *Phys. Rev. A* **2015**, *92*, 023833. [CrossRef]
74. Ndagano, B.; Sroor, H.; McLaren, M.; Rosales-Guzmán, C.; Forbes, A. Beam quality measure for vector beams. *Opt. Lett.* **2016**, *41*, 3407–3410. [CrossRef] [PubMed]
75. Allen, L.; Beijersbergen, M.W.; Spreeuw, R.J.; Woerdman, J.P. Orbital angular momentum of light and the transformation of Laguerre–Gaussian laser modes. *Phys. Rev. A* **1992**, *45*, 8185–8189. [CrossRef] [PubMed]
76. Andrews, L.C.; Phillips, R.L. *Laser Beam Propagation Through Random Media*, 2nd ed.; SPIE Press: Bellingham, WA, USA, 2005.
77. Dong, Z.; Yuan, B.; Liu, Y.; Wang, F.; Cai, Y.; Chen, Y. Stokes scintillations for vector beams in turbulence. *Chin. Opt. Lett.* **2023**, *21*, 100101. [CrossRef]
78. Bachmann, D.; Isoard, M.; Shatokhin, V.; Sorelli, G.; Treps, N.; Buchleitner, A. Highly transmitting modes of light in dynamic atmospheric turbulence. *Phys. Rev. Lett.* **2023**, *130*, 073801. [CrossRef] [PubMed]
79. Chen, R.; Dong, Y.; Wang, F.; Cai, Y. Statistical properties of a cylindrical vector partially coherent beam in turbulent atmosphere. *Appl. Phys. B* **2013**, *112*, 247–259. [CrossRef]
80. Dong, Y.; Guo, L.; Liang, C.; Wang, F.; Cai, Y. Statistical properties of a partially coherent cylindrical vector beam in oceanic turbulence. *J. Opt. Soc. Am. A* **2015**, *32*, 894–901. [CrossRef] [PubMed]
81. Cai, Y.; Wang, F.; Zhao, C.; Zhu, S.; Wu, G.; Dong, Y. *Partially Coherent Vector Beams: From Theory to Experiment*; World Scientific: Singapore, 2013.
82. Gori, F.; Santarsiero, M. Devising genuine spatial correlation functions. *Opt. Lett.* **2007**, *32*, 3531–3533. [CrossRef] [PubMed]
83. Martínez-Herrero, R.; Mejías, P.M.; Gori, F. Genuine cross-spectral densities and pseudo-modal expansions. *Opt. Lett.* **2009**, *34*, 1399–1401. [CrossRef] [PubMed]
84. Gori, F.; Ramírez-Sánchez, V.; Santarsiero, M.; Shirai, T. On genuine cross-spectral density matrices. *J. Opt. A Pure Appl. Opt.* **2009**, *11*, 085706. [CrossRef]
85. Friberg, A.T.; Setälä, T. Electromagnetic theory of optical coherence. *J. Opt. Soc. Am. A* **2016**, *33*, 2431–2442. [CrossRef] [PubMed]
86. Prahl, S.A.; Fischer, D.G.; Duncan, D.D. Monte Carlo Green's function formalism for the propagation of partially coherent light. *J. Opt. Soc. Am. A* **2009**, *26*, 1533–1543. [CrossRef] [PubMed]
87. Collins, S.A. Lens-system diffraction integral written in terms of matrix optics. *J. Opt. Soc. Am.* **1970**, *60*, 1168–1177. [CrossRef]
88. Lin, Q.; Cai, Y. Tensor ABCD law for partially coherent twisted anisotropic Gaussian–Schell-model beams. *Opt. Lett.* **2002**, *27*, 216–218. [CrossRef] [PubMed]
89. Wang, F.; Korotkova, O. Convolution approach for beam propagation in random media. *Opt. Lett.* **2016**, *41*, 1546–1549. [CrossRef] [PubMed]
90. Aviñoá, M.; Martínez-Herrero, R.; Carnicer, A. Efficient calculation of highly focused electromagnetic Schell-model beams. *Opt. Express* **2021**, *29*, 26220–26231. [CrossRef] [PubMed]
91. Yan, C.; Li, X.; Cai, Y.; Chen, Y. Three-dimensional polarization state and spin structure of a tightly focused radially polarized Gaussian Schell-model beam. *Phys. Rev. A* **2022**, *106*, 063522. [CrossRef]
92. Zhao, Y.; Hu, Z.; Shen, J.; Zhu, Y.; Liu, Y.; Liu, L.; Cai, Y.; Wang, F.; Chen, Y. Deterministic polarization states in partially coherent vector light beams. *Phys. Rev. A* **2026**, *114*, 023519. [CrossRef]
93. Miao, W.; Zhang, Y.; Gbur, G. Deterministic vortices evolving from partially coherent fields. *Optica* **2023**, *10*, 1173–1180. [CrossRef]
94. Liu, Y.; Xu, S.; Peng, P.; Zhang, Y.; Dai, S.; Chen, Y.; Cai, Y.; Wang, F. Observation of higher-order deterministic optical vortices from random vortex beams. *APL Photonics* **2025**, *10*, 046118. [CrossRef]
95. Hyde, M.W., IV; Basu, S.; Voelz, D.G.; Xiao, X. Experimentally generating any desired partially coherent Schell-model source using phase-only control. *J. Appl. Phys.* **2015**, *118*, 093102. [CrossRef]
96. Hyde, M.W., IV. Stochastic complex transmittance screens for synthesizing general partially coherent sources. *J. Opt. Soc. Am. A* **2020**, *37*, 257–264. [CrossRef] [PubMed]
97. Zhu, Y.; Dong, Z.; Wang, F.; Chen, Y.; Cai, Y. Compact generation of robust Airy beam pattern with spatial coherence engineering. *Opt. Lett.* **2022**, *47*, 2846–2849. [CrossRef] [PubMed]
98. Dong, Z.; Zhu, Y.; Liu, Y.; Wang, F.; Cai, Y.; Setälä, T.; Chen, Y. Compact generation of light beams carrying robust higher-order Poincaré polarization states. *Appl. Phys. Lett.* **2023**, *122*, 221101. [CrossRef]
99. Zhang, R.; Zhang, M.; Dong, Z.; Wang, F.; Cai, Y.; Chen, Y. Synthesis of robust full Poincaré polarization states via spatial coherence engineering. *Photonics* **2024**, *11*, 286. [CrossRef]
100. Zhu, X.; Yu, J.; Chen, Y.; Wang, F.; Korotkova, O.; Cai, Y. Experimental synthesis of random light sources with circular coherence by digital micromirror device. *Appl. Phys. Lett.* **2020**, *117*, 121102. [CrossRef]

101. Zhu, X.; Yu, J.; Wang, F.; Chen, Y.; Cai, Y.; Korotkova, O. Synthesis of vector nonuniformly correlated light beams by a single digital micromirror device. *Opt. Lett.* **2021**, *46*, 2996–2999. [CrossRef] [PubMed]
102. Zhu, X.; Yu, J.; Chen, Y.; Wang, F.; Cai, Y. Generation of stochastic structured light beams with controllable beam parameters. *ACS Photonics* **2023**, *10*, 2272–2279. [CrossRef]
103. Zhu, X.; Ni, F.; Liu, H.; Yu, J.; Wang, F.; Cheng, Y.; Chen, X.; Cai, Y. High-speed optical coherence manipulation based on a lithium-niobate-film modulator. *PhotoniX* **2025**, *6*, 17. [CrossRef]
104. Partanen, H.; Hoenders, B.J.; Friberg, A.T.; Setälä, T. Young's interference experiment with electromagnetic narrowband light. *J. Opt. Soc. Am. A* **2018**, *35*, 1379–1384. [CrossRef] [PubMed]
105. Arimoto, H.; Ohtsuka, Y. Measurements of the complex degree of spectral coherence by use of a wave-front-folded interferometer. *Opt. Lett.* **1997**, *22*, 958–960. [CrossRef] [PubMed]
106. Dong, Z.; Huang, Z.; Chen, Y.; Wang, F.; Cai, Y. Measuring the complex correlation matrix of partially coherent vector light via a generalized Hanbury Brown–Twiss experiment. *Opt. Express* **2020**, *28*, 20634–20644. [CrossRef] [PubMed]
107. Dai, S.; Wang, Y.; Wang, F.; Chen, Y.; Cai, Y.; Liu, Y. Tomography of complex coherence–polarization matrix of random vector light for phase-image encoding. *ACS Photonics* **2025**, *12*, 6182–6190. [CrossRef]
108. Saastamoinen, K.; Leppänen, L.-P.; Vartiainen, I.; Friberg, A.T.; Setälä, T. Spatial coherence of light measured by nanoscattering. *Optica* **2018**, *5*, 67–70. [CrossRef]
109. Dong, Z.; Saastamoinen, K.; Norrman, A.; Chen, Y.; Friberg, A.T.; Setälä, T. Invariance properties and measurement of correlation between two propagating or evanescent waves. *Laser Photonics Rev.* **2026**, *Early View*. [CrossRef]
110. Liu, Y.; Dong, Z.; Zhu, Y.; Wang, H.; Wang, F.; Chen, Y.; Cai, Y. Three-channel robust optical encryption via engineering the coherence Stokes vector of partially coherent light. *PhotoniX* **2024**, *5*, 8. [CrossRef]
111. Liu, X.; Li, X.; Ponomarenko, S.A.; Wang, F.; Peng, X.; Cai, Y.; Liang, C. Unlocking secure optical multiplexing with spatially incoherent light. *Laser Photonics Rev.* **2025**, *19*, 2401534. [CrossRef]
112. Redding, B.; Choma, M.A.; Cao, H. Speckle-free laser imaging using random laser illumination. *Nat. Photonics* **2012**, *6*, 355–359. [CrossRef] [PubMed]
113. Peng, Y.; Choi, S.; Kim, J.; Wetzstein, G. Speckle-free holography with partially coherent light sources and camera-in-the-loop calibration. *Sci. Adv.* **2021**, *7*, eabg5040. [CrossRef] [PubMed]
114. Xu, D.; Chen, Q.; Zhang, Z.; Liu, J.; Liang, C.; Cai, Y.; Liu, X. Incoherent structured light enabled crosstalk-suppressed 3D volumetric display. *Laser Photonics Rev.* **2026**, *Early View*. [CrossRef]
115. Peng, D.; Huang, Z.; Liu, Y.; Chen, Y.; Wang, F.; Ponomarenko, S.A.; Cai, Y. Optical coherence encryption with structured random light. *PhotoniX* **2021**, *2*, 6. [CrossRef] [PubMed]
116. Lin, S.; Zhu, X.; Shen, Y.; Wang, F.; Chen, X.; Gbur, G.; Cai, Y.; Yu, J. Statistically stationary random light for high-security encryption. *Optica* **2025**, *12*, 1261–1268. [CrossRef]

Disclaimer/Publisher's Note: The statements, opinions and data contained in all publications are solely those of the individual author(s) and contributor(s) and not of MDPI and/or the editor(s). MDPI and/or the editor(s) disclaim responsibility for any injury to people or property resulting from any ideas, methods, instructions or products referred to in the content.